(4)

GL-TR-89-0121

A Study of Spacecraft Electromagnetic Contamination of Artificial Electron Beams

C. S. Lin

Southwest Research Institute
P.O. Drawer 28510
San Antonio, TX 78284

31 December 1988

Final Report
1 August 1987-31 September 1988

GEOPHYSICS LABORATORY
AIR FORCE SYSTEMS COMMAND
UNITED STATES AIR FORCE
HANSCOM AIR FORCE BASE, MASSACHUS 01731-5000

Unclassified

SECURITY CLASSIFICATION OF THIS PAGE (When Data Entered)

REPORT DOCUMENTATION PAGE		READ INSTRUCTIONS BEFORE COMPLETING FORM
1. REPORT NUMBER GL-TR-89-0121	2. GOVT ACCESSION NO.	3. RECIPIENT'S CATALOG NUMBER
4. TITLE (and Subtitle) A Study of Spacecraft Electromagnetic Contamination of Artificial Electron Beams		5. TYPE OF REPORT & PERIOD COVERED FINAL REPORT 1 August 87-31 September 88 6. PERFORMING ORG. REPORT NUMBER
7. AUTHOR(s) C. S. Lin		8. CONTRACT OR GRANT NUMBER(s) F19628-85-K0004
9. PERFORMING ORGANIZATION NAME AND ADDRESS Southwest Research Institute P.O. Drawer 28510 San Antonio, TX 78284		10. PROGRAM ELEMENT PROJECT, TASK AREA & WORK UNIT NUMBERS 61102F 2311G2HE
11. CONTROLLING OFFICE NAME AND ADDRESS		12. REPORT DATE 31 December 1988 13. NUMBER OF PAGES 54
14. MONITORING AGENCY NAME & ADDRESS(if different from Controlling Office) Geophysics Laboratory Hanscom AFB, MA 01731-5000 Contract Manager: William Burke/PHA		15. SECURITY CLASS. (of this report) Unclassified 15a. DECLASSIFICATION/DOWNGRADING SCHEDULE

16. DISTRIBUTION STATEMENT (of this Report)

APPROVED FOR PUBLIC RELEASE; DISTRIBUTION UNLIMITED

17. DISTRIBUTION STATEMENT (of the abstract entered in Block 20, if different from Report)

18. SUPPLEMENTARY NOTES

19. KEY WORDS (Continue on reverse side if necessary and identify by block number)

Electromagnetic Dispersion Equation
Numerical Code
Finite-Size Beam

20. ABSTRACT (Continue on reverse side if necessary and identify by block number)

This report documents the numerical code developed for solving the dispersion equation of the electromagnetic dispersion equation for a finite radius electron beam in a neutralizing background. Derivation of the dispersion equation from the fluid equation and Maxwell's equations is described. To study electromagnetic radiation induced by electron beam injection from the Space Shuttle, the numerical code is applied to solve for the instability growth rates for the beam and whistler modes. The numerical solutions indicate that a finite-radius electron beam injected into the ionosphere with

(Cont.)

DD FORM 1 JAN 73 1473 EDITION OF 1 NOV 65 IS OBSOLETE

Unclassified

SECURITY CLASSIFICATION OF THIS PAGE (When Data Entered)

20. the beam energy around 1 keV and current about 100 mA can drive the beam and whistler modes unstable. The results can explain the whistler waves radiated from the keV electron beam injected from Spacelab 2.

Table of Contents

I. Introduction

Recently active experiments from rockets and the Space Shuttle have been conducted to study beam propagation, spacecraft charging, instabilities, wave emission, and other space plasma phenomena. There experiments indicate that artificial electron beams with energy of several keV and currents about 100 mA produce strong plasma heating and electromagnetic radiation in the whistler frequency range. Although beam-plasma interactions for a finite-radius beam system are well known for electrostatic waves, electromagnetic instabilities of a finite-radius beam system have not been extensively studied because of their complexity.

In this study we focused on the electromagnetic instabilities of a finite-radius electron beam in a neutralizing background. This report gives the derivation of the electromagnetic dispersion equation for the finite-radius beam system and documents the numerical code developed for solving the dispersion equation. Appendix A presents a study of electrostatic instabilities of a finite-radius beam system.

II. Background

Electron beam injection experiments have been conducted from rockets and the Space Shuttle to study beam propagation, instabilities, wave emission, and other space plasma phenomena in the ionosphere [Winkler, 1980; Grandel, 1982; Shawhan *et al.*, 1984; Obayashi *et al.*, 1984]. Experiments have shown that electron beams can generate intense waves of a broad frequency range. For example, during the Spacelab 1 mission, electron beams, which were fired from the Shuttle with a beam energy up to 8 keV and a beam current up to 300 mA, produced broadband emissions at frequencies less than the electron cyclotron frequency ($\omega < \Omega_e$) with both electric and magnetic components [Beghin *et al.*, 1984; Taylor *et al.*, 1985]. During the Spacelab 2 mission, the Plasma Diagnostics Package (PDP), flying around the Shuttle at distances of up to 300 meters, again detected broadband emissions from Ω_e at about 1 Mz down to 30 kHz while the shuttle emitted an electron beam with a beam energy of 1 keV and current of 50 mA [Gurnett *et al.*, 1986]. With both electric and magnetic components, the broadband emissions had a clear funnel shape in the frequency-time spectrogram similar to the auroral hiss reported by Gurnett *et al.* [1983]. Using ray-tracing argument, Gurnett *et al.* [1986] suggested that the broadband emissions are whistler mode radiation from the electron beam.

Several studies have attempted to explain how to produce the broadband whistle radiation by a several keV electron beam. By calculating the radiated power, Farrell *et al.* [1988] proposed that the electron beam generated the radiation through a coherent process, since the measured wave power is several orders higher than the power expected from incoherent Cerenkov radiation. They further suggested that electron bunches created by an electrostatic beam-plasma instability radiate the whistle mode noise. However, they have not shown how the electron beam can excite the electrostatic beam-plasma instability below the cyclotron frequency.

Solving the electrostatic dispersion equation of a finite-size beam for parameters relevant to the Spacelab experiments, we previously found that the beam-plasma instability can generate broadband electrostatic beam mode with frequencies below the electron cyclotron frequency [Lin and Wong, 1986]. The maximum growth rate of the beam mode in this

frequency range is about $10^{-3}\omega_{pe}$. To explain whistler wave emissions, we suggested that the broadband electrostatic waves convert to whistler waves at the electron beam edge. Recently, a computer simulation using an electromagnetic particle code showed that a spatially confined thin electron beam can directly excite whistle mode waves near the resonance cone through Landau resonance [Omura and Matsumoto, 1988]. This simulation also suggested that bunched electrons could not radiate oblique whistler waves because large amplitude electrostatic waves destroy the bunching in a short time during the quasilinear phase.

The objective of this study is to investigate the various wave modes that can be excited by a finite-radius electron beam, with an emphasis on wave frequencies below the electron cyclotron frequency. To achieve this objective, we solved the electromagnetic dispersion equation of a finite-radius beam immersed in a uniform background plasma. For comparison purposes, we also solved the dispersion equation of a homogeneous beam. The numerical solutions indicate that a keV electron beam can drive the beam and whistler modes unstable, regardless of whether the beam is homogeneous or has a finite-radius. Although the beam mode is excited for frequencies up to the electron plasma frequency, only waves with frequencies below the electron cyclotron frequency can propagate outside the beam. The parallel wavenumbers of the whistler waves excited by the finite-radius and the homogenous electron beams are similar, suggesting that the finite-radius electron beam also excites the whistler waves near the resonance cone. These results explain that a very narrow electron beam, such as those of the Spacelab experiments, can still excite whistler waves in the resonance cone.

III. Formulation

A. Basic Equations

This section describes the derivation of the dispersion equation of a finite-radius electron beam in a uniform cold background plasma. We assume that the ambient magnetic field $\vec{B}_o = B_o\hat{z}$ is in the z-direction and that the electron beam propagates along the magnetic field.

We consider an electron beam with a density n_b and a radius r_a centered at the origin $r = 0$. We assume the background electrons have a density n_o outside the beam and $n_c = (n_o - n_b)$ inside the beam so that the background ions distribute uniformly, as illustrated in Figure 1. The relevant equations are the fluid equations

$$\frac{\partial n_j}{\partial t} + \nabla \cdot (n_j \vec{V}_j) = 0 \tag{1}$$

$$\frac{\partial \vec{V}_j}{\partial t} + \vec{V}_j \cdot \nabla \vec{V}_j = -\frac{e}{m}(\vec{E} + \vec{V}_j \times (\vec{B}_o + \vec{B})) \tag{2}$$

and the Maxwell equations

$$\nabla \times \vec{E} = -\frac{1}{c}\frac{\partial \vec{B}}{\partial t} \tag{3}$$

$$\nabla \times \vec{B} = \frac{1}{c}\frac{\partial \vec{E}}{\partial t} + \frac{4\pi}{c}\sum_j e_j n_j \vec{V}_j \tag{4}$$

$$\nabla \cdot \vec{E} = 4\pi \sum_j e_j n_j \tag{5}$$

$$\nabla \cdot \vec{B} = 0 \tag{6}$$

where n_j and $\vec{V}_j$ are the number density and velocity of species j, respectively. Here the index $j = b, p$ refers to the beam and background electrons, respectively. For the background electrons, $v_{op} = 0$.

The electromagnetic dispersion equation of a finite-radius beam has been derived by Shoucri and Kitsenko [1968]. Here, we briefly outline the procedure for obtaining the

dispersion equation. To linearize (1)-(6), we assume

$$\begin{aligned}
\vec{V}_j &= v_{oj}\hat{z} + \delta\vec{v}_j \\
\vec{B} &= B_o\hat{z} + \delta\vec{B} \\
\vec{E} &= \delta\vec{E} \\
n_j &= n_j(r)
\end{aligned}$$

where the zeroth order velocity v_j is constant and in the magnetic field direction. For the background electrons, $V_{op} = 0$. In the derivation given below, we define $\Omega_e = (|e|B_o)/(m_e c)$, and $\omega_{pj}^2 = (4\pi n_j e^2)/m_e$. Using the cylindrical coordinates, we represent the perturbed quantities δf as

$$\delta f = \delta\tilde{f}(r)e^{i(k_\parallel z - \omega t - m\theta)}$$

where $k_\parallel$ is the parallel wave number, θ is the azimuthal angle, and m is an integer. Equations (1)-(2) then become

$$i(\omega - k_\parallel v_{oj})\delta\tilde{n}_j = \frac{n_j}{r}\frac{\partial}{\partial r}(r\delta\tilde{v}_{jr}) + ik_\parallel n_j\delta\tilde{v}_{jz} + i\frac{mn_j}{r}\delta\tilde{v}_{j\theta} + \delta\tilde{v}_{jr}\frac{\partial n_j}{\partial r} \tag{7}$$

$$-i(\omega - k_\parallel v_{oj})\delta\tilde{v}_{jr} = \frac{e}{m}\left[\delta\tilde{E}_r - \frac{1}{c}v_{oj}\delta\tilde{B}_\theta + \frac{1}{c}\delta\tilde{v}_{j\theta}B_\theta\right] \tag{8}$$

$$-i(\omega - k_\parallel v_{oj})\delta\tilde{v}_{j\theta} = \frac{e}{m}\left[\delta\tilde{E}_\theta + \frac{1}{c}v_{oj}\delta\tilde{B}_r - \frac{1}{c}\delta\tilde{v}_{jr}B_o\right] \tag{9}$$

$$-i(\omega - k_\parallel v_{oj})\delta\tilde{v}_{jz} = \frac{e}{m}\delta\tilde{E}_z \tag{10}$$

From (3), we obtain

$$\frac{\delta\tilde{B}_r}{c} = \frac{m}{\omega r}\delta\tilde{E}_z - \frac{k_\parallel}{\omega}\delta\tilde{E}_\theta \tag{11}$$

$$\frac{\delta\tilde{B}_\theta}{c} = \frac{k_\parallel}{\omega}\delta\tilde{E}_r + \frac{i}{\omega}\frac{\partial}{\partial r}\delta\tilde{E}_z \tag{12}$$

Substituting (11) and (12) into (7)-(10), we derive the perturbed velocity quantities as

$$\delta\tilde{v}_{jr} = R_{jr}\delta\tilde{E}_r + R_{j\theta}\delta\tilde{E}_\theta + R_{jz}\delta\tilde{E}_z \tag{13}$$

$$\delta\tilde{v}_{j\theta} = \Theta_{jr}\delta\tilde{E}_r + \Theta_{j\theta}\delta\tilde{E}_\theta + \Theta_{jz}\delta\tilde{E}_z \quad (14)$$

$$\delta\tilde{v}_{jz} = Z_{jz}\delta\tilde{E}_z \quad (15)$$

where

$$\begin{aligned}
R_{jr} &= \frac{ie}{m\omega}\frac{(\omega - k_\parallel v_{oj})^2}{(\omega - k_\parallel v_{oj})^2 - \Omega_e^2} \\
R_{j\theta} &= -\frac{e\Omega}{mw}\frac{(\omega - k_\parallel v_{oj})}{(\omega - k_\parallel v_{oj})^2 - \Omega^2} \\
R_{jz} &= \frac{e}{m\omega}\frac{v_{oj}}{(\omega - k_\parallel v_{oj})^2 - \Omega^2}\left[(\omega - k_\parallel v_{oj})\frac{\partial}{\partial r} - \frac{m\Omega}{r}\right] \\
\Theta_{jr} &= -R_{j\theta} \\
\Theta_{j\theta} &= R_{jr} \\
\Theta_{jz} &= \frac{ie}{m\omega}\frac{v_{oj}}{(\omega - k_\parallel v_{oj})^2 - \Omega^2}\left[-\Omega\frac{\partial}{\partial r} + (\omega - k_\parallel v_{oj})\frac{m}{r}\right] \\
Z_{jz} &= \frac{ie}{m}\frac{1}{\omega - k_\parallel v_{oj}}
\end{aligned}$$

The perturbed current density $\delta\tilde{J}$ is defined as

$$\delta\tilde{J} = \sum_j e(\delta n_j v_{oj}\hat{z} + n_j\delta\tilde{v}_j) \quad (16)$$

$$= \vec{\sigma}\cdot\delta\tilde{E} \quad (17)$$

where $\vec{\sigma}$ is the conductivity tensor. The dielectric tensor is

$$\epsilon_{ij} = \delta_{ij} - \frac{4\pi}{i\omega}\sigma_{ij} \quad (18)$$

Substituting (7), (13)-(15) into (18), we get the expression for the dielectric components

$$\begin{aligned}
\epsilon_{rr} &= 1 - \sum_j \frac{\omega_{pj}^2}{\omega^2}\frac{(\omega - k_\parallel v_{oj})^2}{(\omega - k_\parallel v_{oj})^2 - \Omega^2} \\
\epsilon_{r\theta} &= -\sum_j \frac{i\omega_{pj}^2}{\omega^2}\frac{\Omega(\omega - k_\parallel v_{oj})^2}{(\omega - k_\parallel v_{oj})^2 - \Omega^2} \\
\epsilon_{rz} &= \sum_j \frac{i\omega_{pj}^2}{\omega^2}\frac{v_{oj}}{(\omega - k_\parallel v_{oj})^2 - \Omega^2}\left[(\omega - k_\parallel v_{oj})\frac{\partial}{\partial r} - \frac{m\Omega}{r}\right]
\end{aligned}$$

$$
\begin{aligned}
\epsilon_{zr} &= \sum_j \frac{i}{\omega^2}\frac{v_{oj}}{(\omega - k_\parallel v_{oj})^2 - \Omega^2}\left[\frac{(\omega - k_\parallel v_{oj})}{r}\frac{\partial}{\partial r}(r\omega_{pj}^2) + \frac{m\Omega}{r}\omega_{pj}^2\right] \\
\epsilon_{z\theta} &= -\sum_j \frac{v_{oj}}{\omega^2[(\omega - k_\parallel v_{oj})^2 - \Omega^2]}\left[\frac{\Omega}{r}\frac{\partial}{\partial r}(r\omega_{pj}^2) + \frac{m}{r}\omega_{pj}^2(\omega - k_\parallel v_{oj})\right] \\
\epsilon_{zz} &= 1 - \sum_j \frac{\omega_{pj}^2}{(\omega - k_\parallel v_{oj})^2} + \sum_j \frac{v_{oj}^2}{\omega^2[(\omega - k_\parallel v_{oj})^2 - \Omega^2]} \\
&\quad \left[\frac{1}{r}\frac{\partial}{\partial r}r\omega_{pj}^2\frac{\partial}{\partial r} - \frac{m^2\omega_{pj}^2}{r^2} + \frac{m\Omega}{r(\omega - k_\parallel v_{oj})}\omega_{pj}^2\frac{\partial}{\partial r} - \frac{m\Omega}{(\omega - k_\parallel v_{oj})}\frac{1}{r}\frac{\partial}{\partial r}\omega_{pj}^2\right] \\
\epsilon_{\theta r} &= -E_{r\theta} \\
\epsilon_{\theta\theta} &= E_{rr} \\
\epsilon_{\theta z} &= \sum_j \frac{\omega_{pi}^2}{\omega^2}\frac{v_{oj}}{(\omega - k_\parallel v_{oj})^2 - \Omega^2}\left[\Omega\frac{\partial}{\partial r} - (\omega - k_\parallel v_{oj})\frac{m}{r}\right]
\end{aligned}
$$

B. Normal Components

Suhl and Walker (1954) had expressed the system of equations in terms of the tangential compounds of the electric and magnetic fields $\delta\tilde{E}_z$ and $\delta\tilde{B}_z$. For the axially symmetric plasma oscillations in a cylindrical geometry, we express below the normal components of $\delta\tilde{E}$ and $\delta\tilde{B}$ through $\delta\tilde{E}_z$ and $\delta\tilde{B}_z$.

We first linearize (4) and (6) to obtain

$$\frac{im}{r}\delta\tilde{B}_z - ik_\parallel\delta\tilde{B}_\theta = -i\frac{\omega}{c}\sum_j \epsilon_{rj}\delta\tilde{E}_j \tag{19}$$

$$ik_\parallel\delta\tilde{B}_r - \frac{\partial}{\partial r}\delta\tilde{B}_z = -i\frac{\omega}{c}\sum_j \epsilon_{\theta j}\delta\tilde{E}_j \tag{20}$$

$$\frac{1}{r}\frac{\partial}{\partial r}(r\delta\tilde{B}_\theta) - \frac{im}{r}\tilde{B}_r = -i\frac{\omega}{c}\sum_j \epsilon_{zj}\delta\tilde{E}_j \tag{21}$$

$$\frac{1}{r}\frac{\partial}{\partial r}(r\delta\tilde{B}_z) + \frac{im}{r}\delta\tilde{B}_\theta + ik_\parallel\delta\tilde{B}_z = 0 \tag{22}$$

Substituting (11) and (12) into (19) and (20), we get

$$\begin{pmatrix} -i\frac{\omega}{c}\epsilon_{rr} + i\frac{k_\parallel^2 c}{\omega} & -i\frac{\omega}{c}\epsilon_{r\theta} \\ -i\frac{\omega}{c}\epsilon_{\theta r} & -i\frac{\omega}{c}\epsilon_{\theta\theta} + i\frac{k_\parallel^2 c}{\omega} \end{pmatrix} \begin{pmatrix} \delta\tilde{E}_r \\ \delta\tilde{E}_\theta \end{pmatrix} \tag{23}$$

$$= \begin{pmatrix} i\frac{\omega}{c}\epsilon_{rz} + \frac{k_\parallel c}{\omega}\frac{\partial}{\partial r} & \frac{im}{r} \\ i\frac{\omega}{c}\epsilon_{\theta z} + \frac{ik_\parallel cm}{\omega r} & -\frac{\partial}{\partial r} \end{pmatrix} \begin{pmatrix} \delta\tilde{E}_z \\ \delta\tilde{B}_z \end{pmatrix}$$

Solving (23), we derive

$$\begin{aligned} \delta\tilde{E}_r &= \frac{1}{X^2+Y^2}\left[(XZ_1 - YZ_2)\delta\tilde{E}_z + (iX\frac{m}{r} + Y\frac{\partial}{\partial r})\delta\tilde{B}_z\right] \\ \delta\tilde{E}_\theta &= \frac{1}{X^2+Y^2}\left[(YZ_1 + XZ_2)\delta\tilde{E}_z + (iY\frac{m}{r} - X\frac{\partial}{\partial r})\delta\tilde{B}_z\right] \end{aligned}$$

where

$$\begin{aligned} X &= -\frac{i\omega}{c}\epsilon_{rr} + i\frac{k_\parallel^2 c}{\omega} \\ Y &= -\frac{i\omega}{c}\epsilon_{r\theta} \\ Z_1 &= \frac{i\omega}{c}\epsilon_{rz} + \frac{k_\parallel c}{\omega}\frac{\partial}{\partial r} \\ Z_2 &= \frac{i\omega}{c}\epsilon_{\theta z} + i\frac{k_\parallel c}{\omega}\frac{m}{r} \end{aligned}$$

Given $\delta\tilde{E}_r$ and $\delta\tilde{E}_\theta$, $\delta\tilde{B}_r$ and $\delta\tilde{B}_\theta$ are deduced from (11) and (12)

$$\begin{aligned} \delta\tilde{B}_r &= -\frac{ic}{\omega}\left(\frac{m}{r}\delta\tilde{E}_z - k_\parallel\delta\tilde{E}_\theta\right) \\ \delta\tilde{B}_\theta &= -\frac{ic}{\omega}\left(ik_\parallel\delta\tilde{E}_r - \frac{\partial}{\partial r}\delta\tilde{E}_z\right) \end{aligned}$$

To make the derivation of the system of equations easier, we rewrite the expressions of $\delta\tilde{E}_r$ and $\delta\tilde{E}_\theta$ using the following definitions:

$$a = 1 - \sum_j \frac{\omega_{pj}^2(\omega - k_\parallel v_{oj})^2}{\omega^2[(\omega - k_\parallel v_{oj})^2 - \Omega_e^2]}$$

$$
\begin{aligned}
b &= -\sum_j \frac{\omega_{pj}^2 k_\| v_{oj}(\omega - k_\| v_{oj})}{\omega^2[(\omega - k_\| v_{oj})^2 - \Omega_e^2]} \\
c_1 &= -\sum_j \frac{\omega_{pj}^2}{(\omega - k_\| v_{oj})^2} + \sum_j \frac{\omega_{pj}^2(\omega - k_\| v_{oj})}{\omega[(\omega - k_\| v_{oj})^2 - \Omega_e^2]} \\
c_2 &= -\sum_j \frac{\omega_{pj}^2 k_\| v_{oj}}{\omega[(\omega - k_\| v_{oj})^2 - \Omega_e^2]} \\
d &= \sum_j \frac{\omega_{pj}^2 \Omega_e(\omega - k_\| v_{oj})}{\omega^2[(\omega - k_\| v_{oj})^2 - \Omega_e^2]} \\
f &= -\sum_j \frac{\omega_{pj}^2 \Omega_e k_\| v_{oj}}{\omega^2[(\omega - k_\| v_{oj})^2 - \Omega_e^2]}
\end{aligned}
\tag{24}
$$

From these definitions we get

$$
\begin{aligned}
X &= -\frac{i\omega}{c}(a - N_\|^2) \\
Y &= \frac{\omega}{c} d \\
\epsilon_{rz}\delta\tilde{E}_z &= -\frac{i}{k_\|}\left(b\frac{\partial}{\partial r} + \frac{m}{r}f\right)\delta\tilde{E}_z \\
\epsilon_{\theta z}\delta\tilde{E}_z &= \frac{1}{k_\|}\left(f\frac{\partial}{\partial r} + \frac{m}{r}b\right)\delta\tilde{E}_z
\end{aligned}
$$

where $N_\| = k_\| c/\omega$. The expressions for $\delta\tilde{E}_r$ and $\delta\tilde{E}_\theta$ then become

$$
\delta\tilde{E}_r = \frac{i}{k_\|}\lambda\frac{\partial}{\partial r}\delta\tilde{E}_z - \frac{\mu}{k_\|}\frac{im}{r}\delta\tilde{E}_z + \frac{\xi}{k_\|}\frac{\partial}{\partial r}\tilde{B}_z + \frac{\zeta}{k_\|}\frac{m}{r}\delta\tilde{B}_z \tag{25}
$$

$$
\delta\tilde{E}_\theta = -\frac{m\lambda}{k_\| r}\delta\tilde{E}_z + \frac{\mu}{k_\|}\frac{\partial}{\partial r}\delta\tilde{E}_z + \frac{\xi}{k_\|}\frac{im}{r}\delta\tilde{B}_z + \frac{i\zeta}{k_\|}\frac{\partial}{\partial r}\delta\tilde{B}_z \tag{26}
$$

where

$$
\begin{aligned}
\Gamma &= \left(a - \frac{k_\|^2 c^2}{\omega^2}\right)^2 - d^2 \\
\lambda &= \frac{(a - N_\|^2)(b + N_\|^2) + fd}{\Gamma} \\
\mu &= -\frac{(b + N_\|^2)d + f(a - N_\|^2)}{\Gamma} \\
\xi &= -N_\|\frac{d}{\Gamma}
\end{aligned}
$$

$$\zeta = -\frac{N_{\|}(a - N_{\|}^2)}{\Gamma}$$

We can rewrite $\delta\tilde{B}_\perp$ using (26), as

$$\begin{aligned}
\delta\tilde{B}_\perp &= N_{\|}(\hat{e_{\|}} \times \delta\tilde{E}_\perp) + \frac{iN_{\|}}{k_{\|}}(\hat{e_{\|}} \times \nabla_\perp \delta\tilde{E}_z) \\
&= \frac{iN_{\|}(\lambda+1)}{k_{\|}}(\hat{e_{\|}} \times \nabla_\perp \delta\tilde{E}_z) - \frac{\mu N_{\|}}{k_{\|}}\nabla_\perp \delta\tilde{E}_z \\
&\quad + \frac{N_{\|}\xi}{k_{\|}}(\hat{e_{\|}} \times \nabla_\perp \delta\tilde{B}_z) - \frac{iN_{\|}}{k_{\|}}\zeta\nabla_\perp \delta\tilde{B}_z
\end{aligned} \tag{27}$$

Equations (25) and (26) can be combined into

$$\begin{aligned}
\delta\tilde{E}_\perp &= \frac{i}{k_{\|}}\lambda\nabla_\perp \delta\tilde{E}_z + \frac{\mu}{k_{\|}}(\hat{e_{\|}} \times \nabla_\perp \delta\tilde{E}_z) + \frac{\xi}{k_{\|}}\nabla_\perp \delta\tilde{B}_z \\
&\quad + \frac{i\zeta}{k_{\|}}(\hat{e_{\|}} \times \nabla_\perp \delta\tilde{B}_z)
\end{aligned} \tag{28}$$

IV. Dispersion Equation

A. System of Equations

We now proceed to derive the equations from the tangential components of Maxwell Equations

$$\delta\tilde{B}_z = -\frac{ic}{\omega}\nabla_\perp \times \delta\tilde{E}_\perp \tag{29}$$

$$\frac{ic}{\omega}\nabla_\perp \times \delta\tilde{B}_\perp = \delta\tilde{D}_z = \epsilon_{zr}\delta\tilde{E}_r + \epsilon_{z\theta}\delta\tilde{E}_\theta + \epsilon_{zz}\delta\tilde{E}_z \tag{30}$$

Taking the curl of (29), we deduce

$$\mu\Delta_\perp\delta\tilde{E}_z + i\zeta\Delta_\perp\delta\tilde{B}_z = i\frac{k_\parallel^2}{N_\parallel}\delta\tilde{B}_z \tag{31}$$

where $\Delta_\perp$ is the Laplacian operator $\Delta_\perp = \frac{1}{r}\frac{\partial}{\partial r}r\frac{\partial}{\partial r} - \frac{m^2}{r^2}$.

Taking the curl of (30) and using (28), we deduce (30) to

$$[-(N_\parallel^2 + b)(\lambda + 1) + c_2]\Delta_\perp\delta\tilde{E}_z + i(N_\parallel^2 + b)\xi\Delta_\perp\delta\tilde{B}_z = k_\parallel^2\left[(a + b + c_1)\delta\tilde{E}_z - \frac{if}{N_\parallel}\delta\tilde{B}_z\right] \tag{32}$$

After rewriting (31) and (32), the system of equations is

$$\Delta_\perp\delta\tilde{E}_z + \mathcal{K}\delta E_z + \mathcal{L}\delta B_z = 0 \tag{33}$$

$$\Delta_\perp\delta\tilde{B}_z + \mathcal{P}\delta E_z + \mathcal{Q}\delta B_z = 0 \tag{34}$$

where

$$\mathcal{K} = k_\parallel^2\frac{(a - N_\parallel^2)(a + b + c_1)}{Z}$$

$$\mathcal{L} = -\frac{k_\parallel^2}{N_\parallel}\frac{Y}{Z}$$

$$\mathcal{P} = i\frac{k_{\|}^2}{N_{\|}}\frac{Y}{Z}(a+b+c_1)$$

$$\mathcal{Q} = k_{\|}^2\frac{(a-N_{\|}^2)Z + fY + (b+N_{\|}^2)d(f-d) + c_2d^2}{N_{\|}^2 Z}$$

and

$$Y = (b+N_{\|}^2)d + (a-N_{\|}^2)f$$

$$Z = (b+N_{\|}^2)(a+b) - c_2(a-N_{\|}^2)$$

We next introduce two new variables Ψ_1 and Ψ_2

$$\Psi_1 = \delta E_z + i\Lambda_1 A\delta B_z \tag{35}$$

$$\Psi_2 = \delta E_z + i\Lambda_2 A\delta B_z \tag{36}$$

where Λ_1 and Λ_2 are the roots of the quadratic equation

$$\Lambda^2 + F\Lambda - 1 = 0 \tag{37}$$

The coefficient F is given as

$$\begin{aligned} F = {} & \{N_{\|}^4(c_1-c_2) - N_{\|}^2[a(c_1+b-2c_2) + b^2 + (d-f)^2] \\ & - b(d-f)^2 + (a+b)(ab+f^2) - c_2(a^2-d^2)\}/N_{\|} \\ & / \sqrt{(a+b+c)[(b+N_{\|}^2)d + f(a-N_{\|}^2)]} \end{aligned} \tag{38}$$

The coefficient A is determined from the condition that

$$A^2\mathcal{P} = -\mathcal{L}$$

Hence

$$A = \frac{1}{\sqrt{a+b+c_1}} \tag{39}$$

Multiplying (33) by $i\Lambda A$ and adding it to (34), we obtain

$$\nabla_\perp \Psi_1 + T_1^2 \Psi_1 = 0 \tag{40}$$

$$\nabla_\perp \Psi_2 + T_2^2 \Psi_2 = 0 \tag{41}$$

with

$$T_1^2 = \mathcal{K} + i\Lambda_1 A\mathcal{P} \tag{42}$$

$$T_2^2 = \mathcal{K} + i\Lambda_2 A\mathcal{P}. \tag{43}$$

Using (37), (42) and (43), one can show that T satisifies the equation

$$\begin{aligned} &\frac{(b+N_z^2)(a+b)-(a-N_z)c_2}{N_z^2}T^4 - T^2\frac{K_0^2}{N_z^2}\{-N_z^4(2a+2b+c_1+c_2) \\ &+ N_z^2[a(2a+b+c_1+2c_2)-b^2-(d-f)^2]+(a+b)(ab+f^2) \\ &- b(d-f)^2 - c_2(a^2-d^2)\} + K_0^4(a+b+c_1)[(a-N_z^2)-d^2] = 0 \end{aligned} \tag{44}$$

where $K_0 = \omega/c$. In the case of an unbounded plasma and beam, T corresponds to a normal component of the wave vector $K_\perp$ and to the dispersion equation for an homogenous plasma and beam.

The components δE_z and δB_z are related to the functions Ψ_1 and Ψ_2 by

$$\delta E_z = \frac{\Lambda_2\Psi_1 - \Lambda_1\Psi_2}{\Lambda_2 - \Lambda_1} \tag{45}$$

$$\delta B_z = \frac{i}{A}\frac{\Psi_1 - \Psi_2}{\Lambda_2 - \Psi_1} \tag{46}$$

For axially symmetric oscillations, a solution of (40) and (41) in general has the form

$$\Psi_{1,2} = S_{1,2}J_0(T_{1,2}r) + G_{1,2}Y_0(T_{1,2}r) \tag{47}$$

where J_0 and Y_0 are the Bessel and Neumann functions, respectively. $S_{1,2}$ and $G_{1,2}$ are constants.

B. Boundary Conditions

The boundary conditions are obtained by integrating Maxwell equations across the beam-plasma interface from $r_a - \epsilon$ to $r_a + \epsilon$ with $\epsilon \to 0$. The boundary conditions are

$$\begin{aligned}
\langle \delta E_z \rangle &= 0 \\
\langle \delta E_\theta \rangle &= 0 \\
\langle \delta B_z \rangle &= 0 \\
\langle \delta B_\theta \rangle &= \langle -\frac{c_2}{N_\parallel} \delta E_r \rangle - \langle \frac{b - c_2}{N_\parallel^2} \delta B_\theta \rangle \\
&\quad - \frac{i}{N_\parallel} \left\langle \sum_j \frac{\omega_{pj}^2 \Omega_e^2 k_\parallel v_{oj}}{\omega(\omega - k_\parallel v_{oj})[(\omega - k_\parallel v_{oj})^2 - \Omega_e^2]} \delta E_\theta \right\rangle \\
&\quad - \frac{i}{N_\parallel^2} \left\langle \sum_j \frac{\omega_{pj}^2 \Omega_e k_\parallel^2 v_{oj}^2}{\omega^2(\omega - k_\parallel v_{oj})[(\omega - k_\parallel v_{oj})^2 - \Omega_e^2]} \delta B_r \right\rangle
\end{aligned} \tag{48}$$

The brackets $\langle\rangle$ denote the difference in the values across the beam surface. For example,

$$\langle \delta E_z \rangle = \delta E_z^O|_{r=r_a+0} - \delta E_z^I|_{r=r_a-0}$$

The superscripts O and I mean the quantity is evaluated outside and inside the beam, respectively. The boundary conditions indicate that δE_z, δE_θ and δB_z are continuous at the beam surface but that δB_θ is not. Using (45) and (46), we write the boundary conditions in terms of the functions Ψ_1 and Ψ_2. The first two boundary conditions mean that the tangential components of the electric fields are continuous at the interface.

$$\begin{aligned}
\langle \frac{\Lambda_2 \Psi_1 - \Lambda_1 \Psi_2}{\Lambda_2 - \Lambda_1} \rangle &= 0 \\
\langle \frac{K_o}{(\Lambda_2 - \Lambda_1) A} \left(\frac{1}{T_1^2} \frac{\partial \Psi_1}{\partial r} - \frac{1}{T_2^2} \frac{\partial \Psi_2}{\partial r} \right) \rangle &= 0 \\
\langle \frac{i}{A} \frac{\Psi_1 - \Psi_2}{\Lambda_2 - \Lambda_1} \rangle &= 0 \\
\langle \frac{i K_o}{(\Lambda_2 - \Lambda_1) A^2} \left(\frac{\Lambda_2}{T_1^2} \frac{\partial \Psi_1}{\partial r} - \frac{\Lambda_1}{T_2^2} \frac{\partial \Psi_2}{\partial r} \right) \rangle &= 0
\end{aligned} \tag{49}$$

Parameters are different inside and outside the beam because density and beam velocity are different (see Figure 1).

C. Dispersion Equation

Because electric and magnetic fields should be finite on the Z axis, the functions $\Psi^I_{1,2}$ inside the beam should be

$$\Psi^I_{1,2} = S^I_{1,2} J_m(T^I_{1,2} r). \tag{50}$$

The fields outside the beam should be free propagating waves at a large distance ($r \to \infty$); therefore, the functions $\Psi^O_{1,2}$ outside the beam are

$$\Psi^O_{1,2} = G^O_{1,2} H^{(1)}_m(T^O_{1,2} r) \tag{51}$$

where $H^{(1)}_m(T^O_{1,2} r)$ is the mth order Hankel function of the first kind. $S^I_{1,2}$ and $G^O_{1,2}$ are constants.

The boundary conditions give four equations for the four constants $S^I_{1,2}$ and $G^O_{1,2}$. Requiring the determinant of these equations to be zero, we obtain the dispersion equation

$$\begin{vmatrix} D_{11} & D_{12} & D_{13} & D_{14} \\ D_{21} & D_{22} & D_{23} & D_{24} \\ D_{31} & D_{32} & D_{33} & D_{34} \\ D_{41} & D_{42} & D_{43} & D_{44} \end{vmatrix} = 0 \tag{52}$$

where

$$\begin{aligned} D_{11} &= \Lambda^I_2 J_m(T^I_1 r) \\ D_{12} &= \Lambda^I_1 J_m(T^I_2 r) \\ D_{13} &= \Lambda^0_2 H^{(1)}_m(T^0_1 r) \\ D_{14} &= \Lambda^0_1 H^{(1)}_m(T^0_2 r) \\ D_{21} &= J_m(T^I_1 r)/A^I \end{aligned}$$

$$
\begin{aligned}
D_{22} &= J_m(T_2^I r)/A^I \\
D_{23} &= H_m^{(1)}(T_1^0 r)/A^0 \\
D_{24} &= H_m^{(1)}(T_2^0 r)/A^0 \\
D_{31} &= q_2^I T_1^I J_m'(T_1^I r) - \frac{m}{r} p_2^I J_m(T_1^I r) \\
D_{32} &= q_1^I T_2^I J_m'(T_2^I r) - \frac{m}{r} p_1^I J_m(T_2^I r) \\
D_{33} &= q_2^0 T_1^0 H_m^{(1)\prime}(T_1^0 r) - \frac{m}{r} p_2^0 H_m^{(1)}(T_1^0 r) \\
D_{34} &= q_1^0 T_2^0 H_m^{(1)\prime}(T_2^0 r) - \frac{m}{r} p_1^0 H_m^{(1)}(T_2^0 r) \\
D_{41} &= g_2^I T_1^I J_m'(T_1^I r) + \frac{m}{r} w_2^I J_m(T_1^I r) \\
D_{42} &= g_1^I T_2^I J_m'(T_2^I r) + \frac{m}{r} w_1^I J_m(T_2^I r) \\
D_{43} &= g_2^0 T_1^0 H_m^{(1)\prime}(T_1^0 r) + \frac{m}{r} w_2^0 H_m^{(1)}(T_1^0 r) \\
D_{44} &= g_1^0 T_2^0 H_m^{(1)\prime}(T_2^0 r) + \frac{m}{r} w_1^0 H_m^{(1)}(T_2^0 r)
\end{aligned}
$$

The dispersion equation (52) contains the variables p_i, q_i, g_i, and w_i, which are defined as

$$
\begin{aligned}
p_{1,2} &= \frac{[(a - N_\parallel^2)(b + N_\parallel^2) + fd]\Lambda_{1,2} - N_\parallel d/A}{(a - N_\parallel^2)^2 - d^2} \\
q_{1,2} &= \frac{k_\parallel \omega}{cAT_{2,1}^2} \\
g_{1,2} &= \frac{k_\parallel \omega \Lambda_{1,2}}{cA^2 T_{2,1}^2} \\
w_{1,2} &= \frac{(b + N_\parallel^2)^2 + 2f(b + N_\parallel^2)(a - N_\parallel^2) + f^2 d - l[(a - N\|^2)^2 - d^2]}{(a - N_\parallel^2)^2 - d^2} \frac{\Lambda_{1,2}}{N_\parallel} \\
&\quad - \frac{1}{A} \frac{(a - N_\parallel^2)(b + N_\parallel^2) + fd}{(a - N_\parallel^2)^2 - d^2}
\end{aligned}
$$

where

$$
l = -\sum_j \frac{\omega_{pj}^2 \Omega_e k_\parallel^2 v_{oj}^2}{\omega^2(\omega - k_\parallel v_{oj})[(\omega - k_\parallel v_{oj})^2 - \Omega_e^2]}
$$

In general, the variables depend on n_j and v_{oj} and thus vary from inside the beam to

outside the beam. We thus use the superscripts I and O to distinguish their values inside and outside the beam, respectively, in Section II.

V. Description of Numerical Code

This section describes the numerical code EMFBP that solves the dispersion equation (52). EMFBP contains the main program and the five subroutines FCN, FSBELEC, JHC, ROOT and DFCN. Although the dispersion equation is quite complicated and requires double precision to evaluate, the structure of this program is simple. The program computes the complex roots of the dispersion equation, which is a complex algebra equation, for given input parameters. The root-solving routine iterates until the error in solving the dispersion equation is less than a prescribed value, 10^{-4}. The program then outputs the root for each k value.

A. Main Program

The main program primarily reads the input variables, which are listed below:

Table 1. List of Input Variables

variable name	definition	typical value
WR2	ω_{pe}/Ω	3
DR	n_b/n_c	0.1
VB1	v_{op}^O/c	0
VB2	v_{op}^I/c	0
VBB	v_{ob}^I/c	0
RBA	$\omega_{pe}r_a/v_{ob}$	0.111
KI	$k_{\|}c/\Omega$	40
DK	$\Delta k_{\|}c/\Omega$	1
NK	number of k mode	10
GR	real (Z)	0.33
GI	Imaginary (Z)	0.05

The variable WR2 is the ratio of the electron plasma frequency to the electron gyrofrequency.

As shown in the density model, the variable DR is the ratio of the beam density to the background density outside the beam. The variables VB1 and VB2 are the drift velocities of the background electrons outside and inside the beam, respectively. In this study, we have assumed VB1 and VB2 to be zero. The variable VBB is the beam velocity in the unit of speed of light. For a 1 keV electron beam, VBB is 0.01. The beam radius defines the normalized variable RBA; for a beam radius of 2 m and a beam energy of 1 keV, RBA is 0.0111. The main program also reads the initial value of $k_{\|}c/\Omega$ for solving the dispersion equation. DK is the increment in $k_{\|}c/\Omega$ and NK is the number of times the program solves the dispersion equation. The program requires an initial guess of the root Z, where Z is ω/Ω. The input variables are contained in a common block /MON/ for passing arguments to other subroutines.

After reading the input variables, the main program calls the subroutine ROOTF, which uses Muller's method for solving a complex algebra equation. In ROOTF, the subroutine calls DFCN for finding the roots and FCN for computing the dispersion equation (52).

B. Computation of the Dispersion Equation

Complex function FCN*16(Z) function computes the dispersion equation (52) for a given Z and returns the result in a complex value. FCN calls two subroutines FSBELEC and JHC. The subroutine FSBELEC computes the electron response terms a, b, c_1, c_2, d, and f, given in Section III A, and l, given in Section IV C.

The subroutine JHC computes the mth order Bessel function $J_m(Z)$ and Hankel function of the first kind $H_m^{(1)}(Z)$. The subroutine JHC has input arguments Z and m, where Z is complex and m is integer. The subroutine computes $J_m(Z)$ and $H_m^{(1)}(Z)$ according to the expressions given in Handbook of Mathematical Functions [Abramowitz and Segun, 1968]. For the absolute value of Z less than 15, the routine uses the series expansion to compute $J_m(Z)$ and $H_m^{(1)}(Z)$. For the absolute value of Z greater than 15, the routine uses Hankel's asymptotic expansion.

VI. Numerical Results

This section describes the numerical solutions of the dispersion equation for a homogeneous beam and for a finite-radius beam. We assumed that the cold electron beam has a beam energy of 1 keV and a density 1% of the ambient density, $n_b/(n_c + n_b) = 0.01$. This assumption was based on the Spacelab 2 experiment parameters, which had a 1-keV, 50-mA electron beam [Gurnett *et al.*, 1986]. The ambient plasma density n_c at the Shuttle altitude is generally near 10^5 cm^{-3}, corresponding to a plasma frequency of 2.85 MHz. Since the Spacelab 2 measured the electron plasma waves near 3 MHz, we assumed the electron plasma frequency to be 3 MHz in solving the dispersion equations. We also used $\omega_e/\Omega_e = 3$ because the electron cyclotron frequency is about 1 MHz. In solving the dispersion equation of a finite-radius beam, we assumed the beam radius to be 2.5 m, according to Gurnett *et al.* [1986].

Figs. 2 and 3 give the solutions of the dispersion equation for the homogeneous beam. Fig. 2 shows the wave frequency ω_r as a function of kc/Ω_e for various wave normal angles. The beam plasma mode has frequencies linearly proportional to kc/Ω_e, intersecting the plasma frequency at $\omega_e/\Omega_e = 3$, as indicated on the vertical axis. The dashed lines in Fig. 2 represent the whistle mode, which has frequencies approaching $\Omega_e \cos\theta$. Fig. 3 gives the growth rate ω_i for both the beam plasma and whistler modes. As expected, the beam plasma mode has a large growth rate, which decreases with angle (solid lines). For example, the maximum value of ω_i/Ω_e is 0.4 for $\theta = 0°$ and 0.25 for $\theta = 60°$. Note that the growth rate of the beam plasma mode at large angles has dropped sharply at certain kc/Ω_e. For example, ω_i/Ω_e for $\theta = 60°$ drops below 10^{-2} for kc/Ω_e between 20 and 32, corresponding to wave frequencies near the electron cyclotron frequency. The decrease in growth rate is due to the cyclotron resonance interactions of the electron beam. Fig. 3 also shows that the cold electron beam can excite whistler waves at large normal angles with smaller growth rates (dashed lines). From Figs. 2 and 3, we note that the frequency of unstable whistler waves occurs at $\Omega_e \cos\theta$ where the frequency is insensitive to k, suggesting that the electron beam excites the whistler mode at the resonance cone. Fig. 3 indicates that the growth rate of the whistler mode is about $0.025\Omega_e$ for $\theta = 60°$ and $0.012\Omega_e$ for $\theta = 30°$. For $\theta = 60°$, this

corresponds to an e-folding time of approximately 6 μs. Although the temporal growth rate of the whistler wave is small in comparison with the beam mode, the spatial amplification of the whistler wave can be significant because of its small group velocity at the resonance cone.

Figs. 4 and 5 give the solutions of the dispersion equation of the finite-radius beam. In solving (52), we restrict our attention to the axially symmetric case (i.e., $m = 0$) only. Since we are mainly interested in waves with frequencies below Ω_e, we have neglected the cyclotronic mode, which has been discussed previously by Le Queau *et al.* [1981]. Because the perpendicular wavenumber is no longer a constant, these figures plot the frequency and growth rate versus the normalized parallel wavenumber $k_{\|}c/\Omega_e$. Like the homogeneous beam case, the finite-radius electron beam is unstable to the beam plasma mode with wave frequency $\omega_r \cong k_{\|}v_{ob}$ (Fig. 4). The growth rate is also large when $k_{\|}c/\Omega_e > 20$, which corresponds to $\omega_r/\Omega_e > 1$. However, except near the electron plasma frequency, the solutions indicate that the argument of the Hankel function for the beam mode has its imaginary part larger than the real part ($|Im(T_j^o r)| > |Re(T_j^o r)|$) when $\omega_r/\Omega_e > 1$ (Fig. 4). This means that the waves with frequencies $\Omega_e < \omega < \omega_e$ are radially confined inside the beam. The reason for the confinement is that the ambient plasma outside the beam does not support a normal mode for $\Omega_e < \omega < \omega_e$. For $\omega < \Omega_e$, the beam mode has a smaller growth rate about $0.01\Omega_e$, but the argument of the Hankel function has a larger real part than imaginary part. Therefore, the beam mode excited with frequencies below Ω_e can propagate away from the beam because the ambient plasma has the whistler mode as its normal mode. The drop in the growth rate at the cyclotron frequency is due to the cyclotron resonance interactions of the electron beam, similar to the homogeneous beam case.

Besides the beam mode, (52) also has solutions for the whistler mode shown in Fig. 5. This figure indicates that the frequency approaches Ω_e for large $k_{\|}c/\Omega_e$. The solutions for $\omega_r/\Omega_e < 0.02$ are near the lower hybrid frequency and thus are not accurate because we have neglected the ion contributions in (52). Although the real frequency appears as a single curve, we have actually obtained several unstable branches, all with very close frequencies

but different growth rates. Fig. 2 indicates that the whistler mode for the homogeneous beam has a frequency for each angle. Therefore, at a given parallel wavenumber, the whistler mode has a continuous frequency spectrum as the perpendicular wavenumber varies. For a finite-radius beam, the perpendicular wavelength inside the beam is quantized and thus the whistler mode has a set of discrete frequencies as shown in Fig. 5. We have plotted two branches with the largest growth rates, which are smaller than the growth rates of the beam mode.

For the finite-radius beam case, one cannot easily determine whether the electron beam excites whistler waves at the resonance cone, since the perpendicular normal vector is not constant. However, we note that $k_{\|}c/\Omega_e$ is the same for the finite-radius and homogeneous beams cases. Fig. 2 indicates that the homogeneous beam excites whistler waves at $k_{\|}c/\Omega_e = 24$ for $kc/\Omega_e = 48$ and $\theta = 60°$, whereas the finite-radius beam excites whistler waves for $k_{\|}c/\Omega_e$ ranging from 18 to 25, according to Fig. 5. The parallel wavelength, therefore, suggests that the finite-radius beam also excites whistler waves near the resonance cone.

VII. Summary

Our numerical calculations indicate that the keV electron beam injected from the Shuttle with a narrow radius can directly excite whistler waves propagating at the resonance cone. This result thus supports the work of Omura and Matsumoto [1988], which showed the direct excitation of whistler waves by using computer simulations. Although the beam mode is excited for frequencies up to the electron plasma frequency, only the waves below the electron cyclotron frequency can propagate outside the beam. As suggested by Farrell *et al.* [1988], the electrostatic waves of the beam mode at the whistler frequencies could bunch electrons, which then radiate whistler waves. However, one cannot rule out the possibility of mode conversion at the beam edge, as proposed by Lin and Wong [1986]. Electrostatic waves of the beam mode could convert into whistler waves at the beam edge due to density discontinuity and propagate away from the beam. Future studies are required to resolve these questions.

References

Beghin, C., J. P. Lebreton, B. N. Maehlum, J. Troim, P. Ingsoy, and J. L. Michau, Phenomena induced by charged particle beams, *Science, 225*, 188, 1984.

Farrell, W. M., D. A. Gurnett, P. M. Banks, R. I. Bush, and W. J. Raitt, An analysis of whistler mode radiation from the Spacelab 2 electron beam, *J. Geophys. Res., 93*, 153, 1988.

Grandal, B. (Ed.), Artificial Particle Beams in Space Plasma Studies, *NATO Adv. Study Intrum. Ser., Ser. B, 79*, 704 pp., 1982.

Gurnett, D. A., S. D. Shawhan, and R. R. Shaw, Auroral hiss, Z mode radiation and auroral kilometric radiation in the polar magnetosphere: DE-1 observations, *J. Geophys. Res., 88*, 329, 1983.

Gurnett, D. A., W. S. Kurth, T. Steinberg, P. M. Banks, R. I. Bush, and W. J. Raitt, Whistler-mode radiation from the Spacelab-2 electron beam, *Geophys. Res. Lett., 13*, 225, 1986.

Le Queau, D., R. Pellat, and A. Saint Marc, Electrostatic instabilities of a finite electron beam propagating in a cold magnetized plasma, *Phys. Rev., A, 24*, 448, 1981.

Lin, C. S., and H. K. Wong, Plasma instabilities of artificial electron beams in the ionosphere, SwRI Preprint, 1986. GL-TR-89-0121 (page 35)

Montgomery, D. C., and D. A. Tidman, *Plasma Kinetic Theory*, McGraw-Hill, New York, 1964.

Obayashi, T., N. Kawashima, K. Kuriki, M. Nagatomo, K. Ninomiya, S. Sasaki, M. Yanagisawa, I. Kudo, M. Ejiri, W. T. Roberts, C. R. Chappell, D. L. Reasoner, J. Burch, W. W. L. Taylor, P. M. Banks, P. R. Williamson, and O. K. Garriott, Space experiments with particle accelerators, *Science, 225*, 195, 1984.

Omura, Y., and H. Matsumoto, Computer experiments of whistler and plasma wave emissions for Spacelab-2 electron beam, *Geophys. Res. Lett., 15*, 319, 1988.

Shawhan, S. D., G. B. Murphy, P. M. Banks, P. R. Williamson and W. J. Raitt, Wave emissions from dc and modulated electron beams on STS-3, *Radio Sci., 19*, 471, 1984.

Shoucri, M. M., and A. B. Kitsenko, Oscillations of bounded beam-plasma systems in cylindrical geometry, *Plasma Phys.*, *10*, 699, 1968.

Taylor, W. W. L., T. Obayashi, N. Kawashima, S. Sasaki, M. Yanagisawa, J. L. Burch, D. L. Reasoner, and W. T. Roberts, Wave-particle interactions induced by SEPAC on Spacelab-1: wave observations, *Radio Sci.*, *20*, 486, 1985.

Winckler, J. R., The application of artificial electron beams to magnetospheric research, *Rev. Geophys.*, *18*, 659, 1980.

Figure Captions

Figure 1. Physical configuration of a finite-radius electron beam immersed in a uniform plasma.

Figure 2. Frequency of the beam mode (solid curve) and the whistler mode (dashed curve) at a given wave normal angle θ as a function of kc/Ω_e.

Figure 3. Growth rate of the beam mode (solid curve) and the whistler mode (dashed curve) at a given wave normal angle θ.

Figure 4. Frequency and growth rate of the beam mode for a finite-radius electron beam as a function of $k_{\|}c/\Omega_e$. The parameters are $n_b/n_c = 0.1$, $E_b = 1\,\mathrm{keV}$, $r_a = 2\,\mathrm{m}$, and $\omega_e/\Omega_e = 3$.

Figure 5. Frequency and growth rate of the whistle mode for a finite-radius electron beam. The parameters are the same as those for Figure 4.

DENSITY MODEL

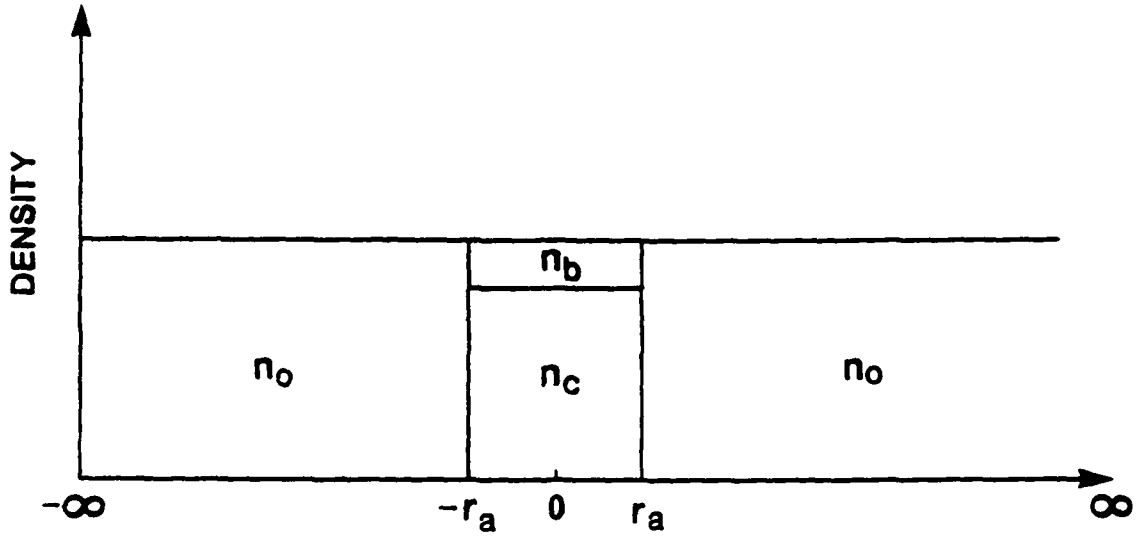

Figure 1

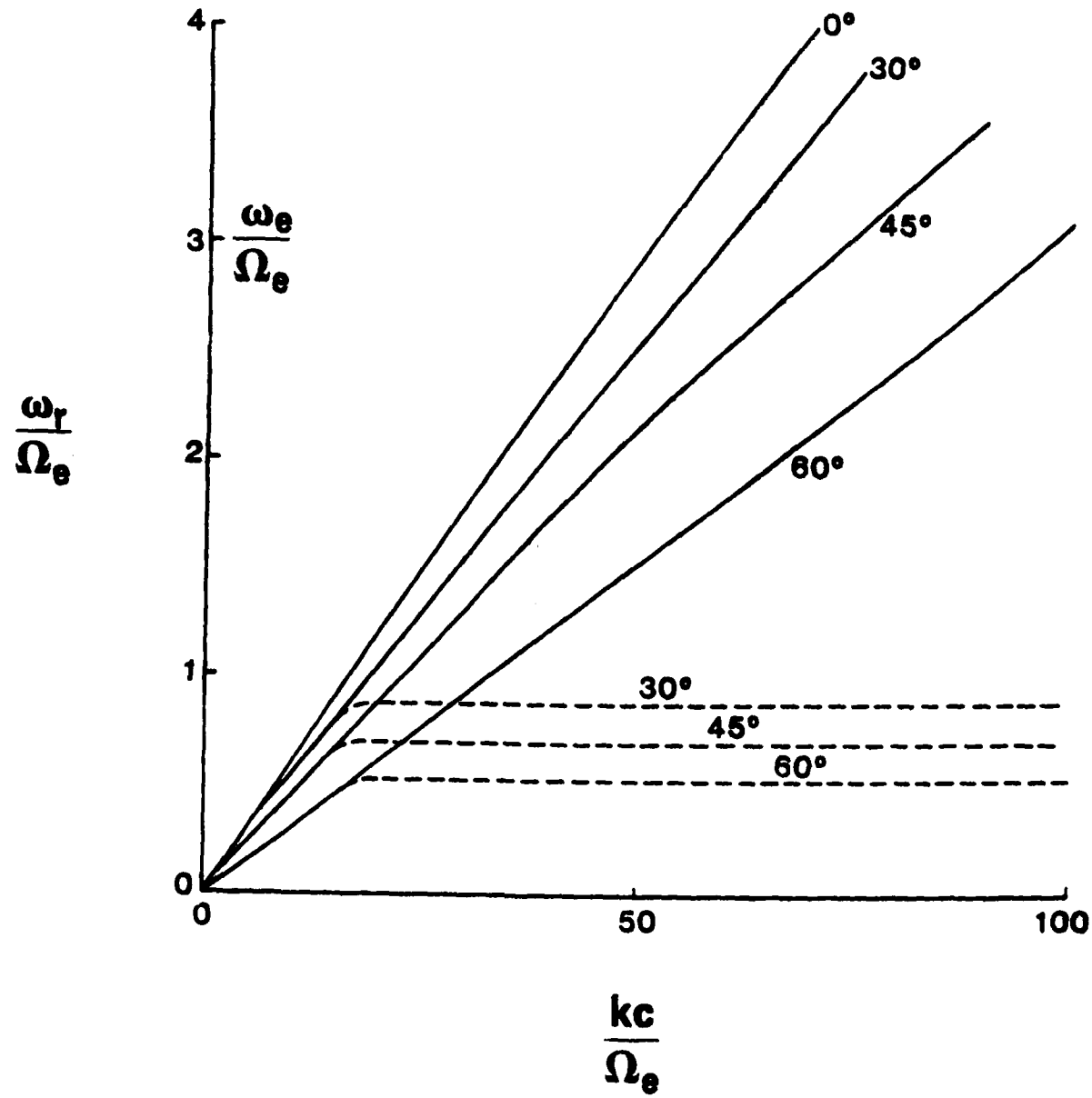

Figure 2

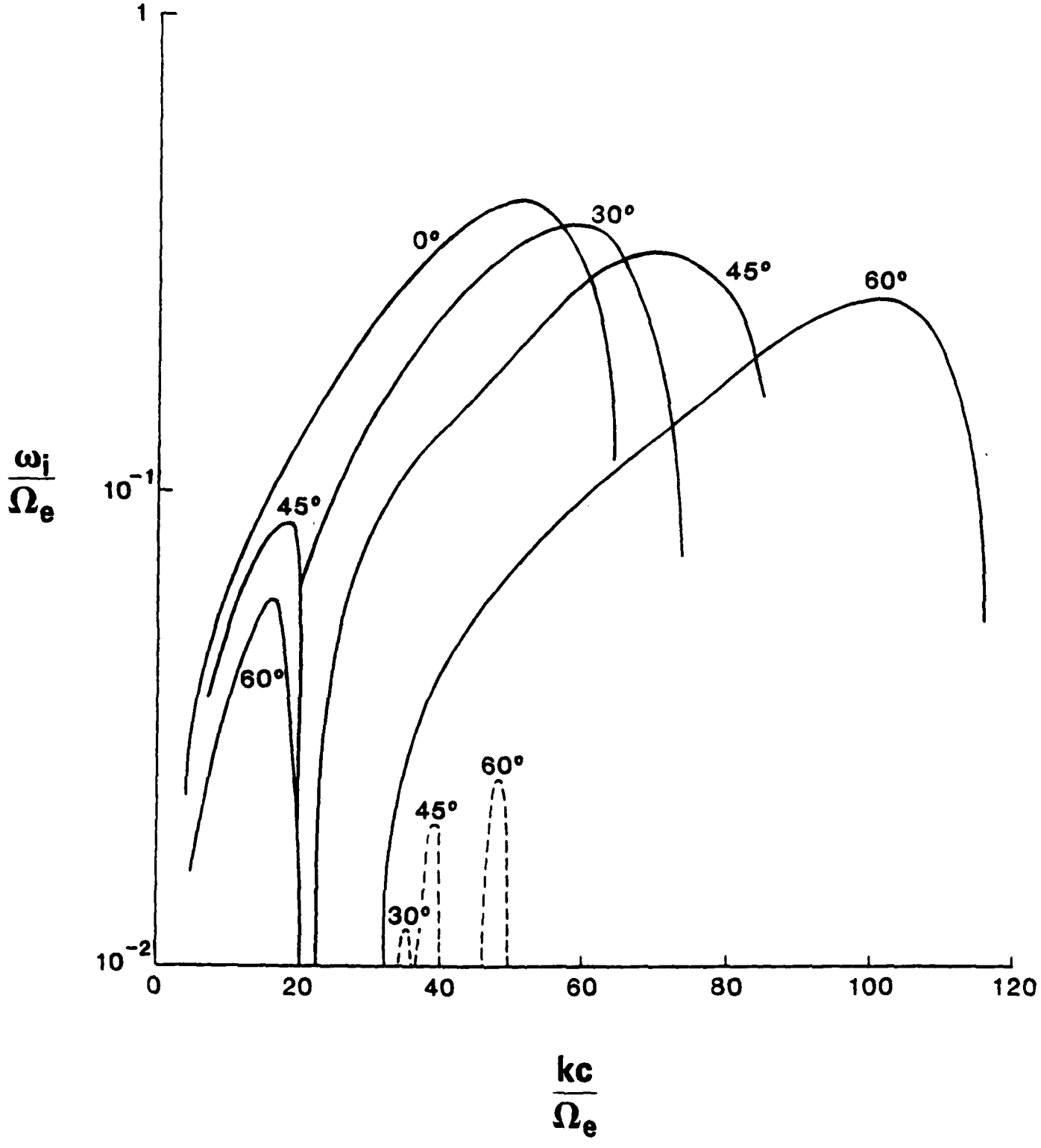
1
10^{-1}
10^{-2}
$\frac{\omega_i}{\Omega_e}$
0°
30°
45°
60°
45°
60°
60°
45°
30°
0
20
40
60
80
100
120
$\frac{kc}{\Omega_e}$

Figure 3

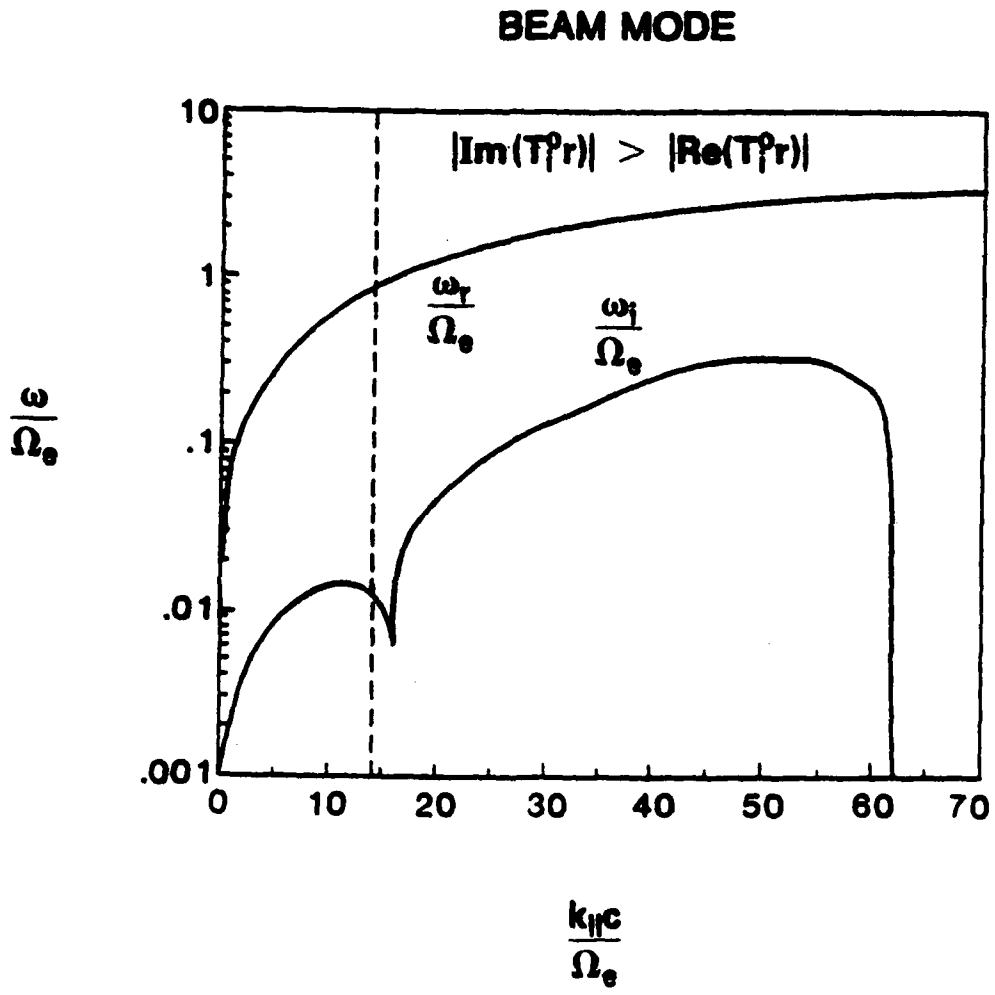
BEAM MODE
|Im(T$_j^0$r)| > |Re(T$_j^0$r)|
$\frac{\omega_r}{\Omega_e}$
$\frac{\omega_i}{\Omega_e}$
$\frac{\omega}{\Omega_e}$
10
1
.1
.01
.001
0
10
20
30
40
50
60
70
$\frac{k_{||}c}{\Omega_e}$

Figure 4

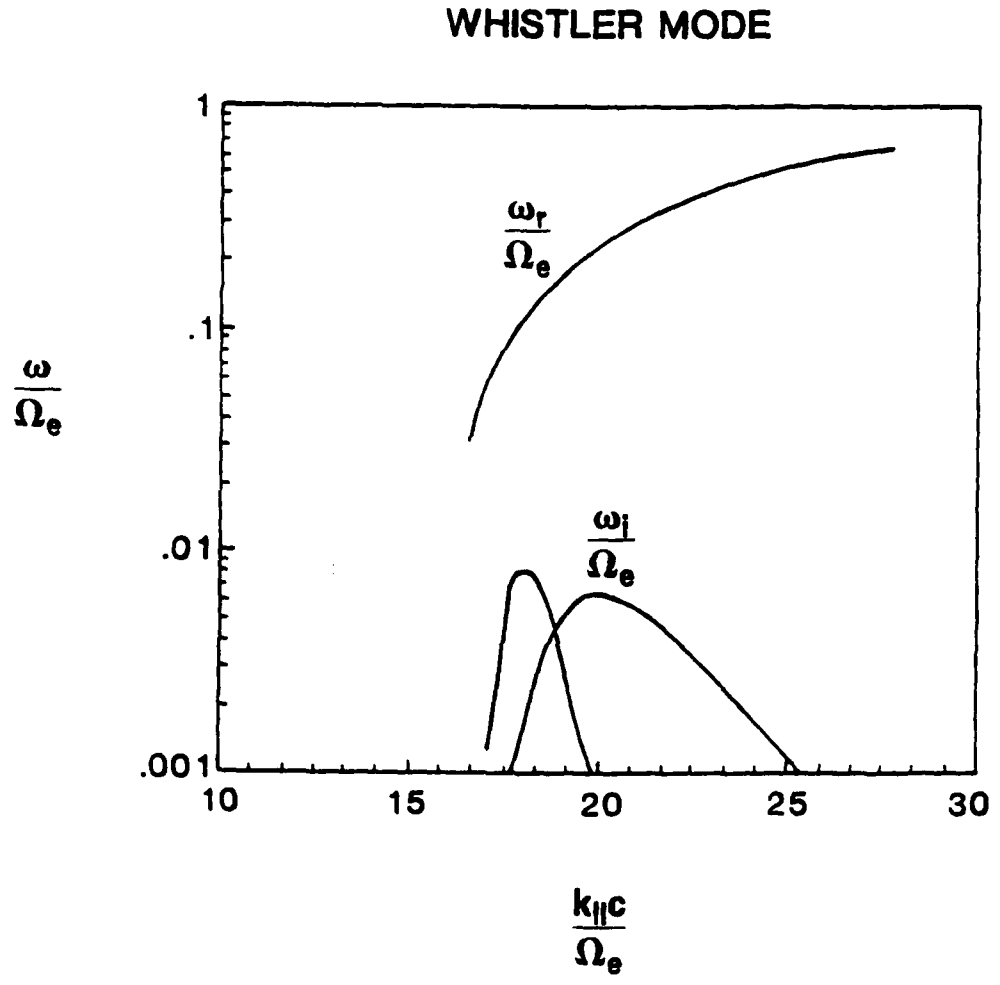

Figure 5

APPENDIX A

Plasma Instabilities of Artificial Electron Beams In the Ionosphere

C. S. Lin
and
H. K. Wong

Department of Space Sciences
Southwest Research Institute
San Antonio, Texas 78284

September 2, 1986

Abstract

The full electromagnetic dispersion equation of a homogeneous beam and the electrostatic dispersion equation of a finite-size electron beam are solved for parameters relevant to DC electron beam experiments conducted from the Space Shuttle. The numerical solutions of the homogeneous dispersion equation indicate that the electron beam mode with frequency $\omega = k_{\|} v_b$ has large growth rates over a wide range of frequencies and angles, whereas whistler waves have small growth rates at frequencies near the electron cyclotron frequency Ω_e. At oblique propagation and at low frequencies ($\omega < 0.1\Omega_e$), the beam mode is coupled to whistler waves and has a significant electromagnetic component. Because of the finite size effects, the electron beam instability has a minimum growth rate at the electron cyclotron frequency. Our results do not favor direct excitation of whistler waves in the ionosphere through linear instabilities of keV electron beams. To explain whistler wave emissions during the Shuttle electron beam experiments, it is suggested that the electron beam first excites broadband electrostatic waves, which are subsequently converted to whistler waves at the beam edge.

1 Introduction

Different types of waves have been observed in association with the DC electron beam emission experiments in the Spacelab 1 and Spacelab 2 missions. During the Spacelab 1 mission, broadband emissions at frequencies less than the electron cyclotron frequency ($\omega < \Omega_e$) with both electric and magnetic components were detected by wave instruments on board the Shuttle during the firing of a 5 keV and 300 mA electron beam (Taylor et al., 1985). During the recent Spacelab 2 mission the Plasma Diagnostics Package (PDP) performed a fly-around of the Shuttle at distances of up to 300 meters while a DC electron beam with a beam energy of 1 keV and current of 50 mA was being emitted from the Shuttle. The PDP detected broadband emissions at $\omega < \Omega_e$ with both electric and magnetic components and a narrow band electrostatic emission near the plasma frequency ω_{pe} (Gurnett et al., 1986). The broadband emissions had a clear funnel shape in the frequency-time spectrogram, similar to the observations of auroral hiss (Gurnett et al., 1983). The broadband emission is believed to be caused by whistler-mode emission from the beam propagating near the resonance cone.

Electron beams are known to radiate whistler waves through spontaneous emissions, but the predicted intensity is generally several orders of magnitude smaller than those observed (Taylor and Shawhan, 1974; Farrell et al., 1986). We therefore examined the stimulated emission of waves through instabilities in the whistler frequency range. Using the experimental parameters, we solved both the general electromagnetic dispersion equation for a homogeneous beam and an electrostatic dispersion equation for a finite-size beam. As expected, the solutions indicate that the beam mode is much more unstable than the whistler mode. A more surprising finding is that the oblique beam mode has a significant electromagnetic component at low frequencies ($\omega < \Omega_e$). Based on the instability analysis, mechanisms that cause artificial electron beams to emit whistler waves in the ionosphere are suggested.

2 Instabilities of a Homogeneous Beam

The electromagnetic dispersion equation for the homogeneous beam plasma system is derived in a representation based on the electrostatic and electromagnetic potentials rather than the electric field. The potential representation is useful for our purposes because it simplifies the separation of the electrostatic and electromagnetic perturbations. Kinetic effects are included since electron beams might be thermalized by beam plasma instabilities after propagation. The dielectric tensor used in the calculation can be transformed into the well known formula of Stix (1962) and is therefore not given here.

The ambient plasma density n_e at the Shuttle altitude is generally near $10^5 cm^{-3}$ corresponding to a plasma frequency of about 2.85 MHz. Since the electron cyclotron frequency is about 1.0 MHz in the ionosphere, we chose the ratio $\omega_{pe}/\Omega_e = 3$ in the calculation for simplicity. The two key parameters in solving the dispersion equation are n_b/N, the ratio of the beam density n_b to the total plasma density N, and V_b/α, the ratio of beam drift velocity V_b to the beam thermal velocity α. The dispersion equation is solved for the ratio of $n_b/N = 0.1$ and $V_b/\alpha = 10$.

Figure 1 shows the normalized wave frequency ω/Ω_e and the normalized growth rate γ/Ω_e of the beam mode as a function of kc/Ω_e for wave normal angle $\theta = 0^0$, 30^0 and 60^0 (solid lines). The parameters $n_b/N = 0.1$ and $V_b/\alpha = 10$ are used. The electron beam mode is unstable for a wide frequency range from zero to $\omega = 3.4\Omega_e$, slightly above the upper hybrid resonance frequency ($3.2\Omega_e$). The maximum growth rate occurs at $\omega = 2.6\Omega_e$ for $\theta = 0^0$. Both the wave frequency and growth rate of the beam mode decrease with θ.

The beam mode not only has a large growth rate but also has a group velocity in the direction near the magnetic field. For $\theta = 30^0$, the angle between the group velocity and the magnetic field is found to be only about 5^o. Therefore, the beam mode can grow to large amplitudes inside the electron beam.

Figure 1 also shows the frequency and growth rate of whistler waves for $\theta = 30^0$ (dotted line). The whistler wave frequency is close to the beam mode frequency for $kc/\Omega_e < 5$. The growth rate of whistler instability is much smaller than the beam mode instability (note that the whistler growth rate has been multiplied by a factor of 100 in Figure 1). The instability occurs at two frequencies, near 0.1 Ω_e and 0.85 Ω_e. The growth rate at $\omega = 0.1\Omega_e$ is very small (only about $0.0002\Omega_e$) and not presentable in the figure. The

Cerenkov resonant energy increases with wave number k to a maximum near $kc/\Omega_e = 5$ and then decreases with k after $kc/\Omega_e > 5$. An electron beam with a beam energy of several keV can resonate with whistler waves at two wave vectors (near 1 and 10 kc/Ω_e) and thus excite whistler waves at two frequencies.

To determine whether the excited wave is electrostatic or electromagnetic, we plot the ratio of the longitudinal electric field component E_L to the total electric field E_T (Figure 2). The ratio E_L/E_T is 1 for purely electrostatic waves and 0 for purely electromagnetic waves. Figure 2 shows that the beam mode is electrostatic for $kc/\Omega_e > 3$ and has a significant transverse electric field component ($E_L/E_T = 0.6$ for $kc/\Omega_e = 1$). For whistler waves at $\theta = 30^0$, E_L/E_T is about 0.4 at kc/Ω_e=1 and about 1 at kc/Ω_e =10. Therefore, the unstable whistler waves become electrostatic for $kc/\Omega_e > 10$. Since the beam mode is generally believed to be electrostatic, it is unexpected that the oblique propagating beam mode has a substantial transverse electric field component at low frequencies. The bottom panel of Figure 2 indicates that the dispersion curves of the beam and whistler modes cross each other at $kc/\Omega_e \approx 1$, suggesting that the electron beam mode couples to whistler waves.

The frequency and growth rate of the beam mode are examined for various values o f n_b/N and v_b/α. The growth rate of the beam mode decreases as the beam density decreases. At sufficiently low density, the beam mode ceases to exist and the instability occurs only at frequencies close to the plasma frequency. The effect of increasing the beam thermal velocity is similar to that of decreasing the beam density.

3 Instability of a Finite-size Electron Beam

The electrostatic dispersion equation of a cold electron beam with a finite radius injected along the magnetic field in a cold uniform plasma has been derived (Le Queau et al., 1981). The electrostatic dispersion equation is

$$T\frac{J_1(T)}{J_0(T)} = U\frac{\epsilon_\perp^{out}}{\epsilon_\perp^{in}}\frac{H_1^{(1)}(U)}{H_0^{(1)}(U)} \tag{1}$$

where J_n is the Bessel function of order n and $H_n^{(1)}$ is the Hankel function of the first kind of order n. The Hankel function is defined in terms of the Bessel function of the first kind J_n and second kind Y_n as $H_n^{(1)} = J_n + iY_n$. The arguments T and U are defined as $T = k_\perp^{in}a$ and $U = k_\perp^{out}a$. Here a is the beam radius; $k_\perp^{in}$ and $k_\perp^{out}$ are the effective perpendicular wave number inside and outside the beam respectively. The following definitions are also used:

$$\begin{aligned}
k_\perp^{in} &= k_\parallel(-\epsilon_\parallel^{in}/\epsilon_\perp^{in})^{\frac{1}{2}} \\
k_\perp^{out} &= k_\parallel(-\epsilon_\parallel^{out}/\epsilon_\perp^{out})^{\frac{1}{2}} \\
\epsilon_\perp^{in} &= 1 - \frac{\omega_{pe}^2}{\omega^2 - \Omega_e^2} - \frac{\delta\omega_{pe}^2}{(\omega - k_\parallel)^2 - \Omega_e^2} \\
\epsilon_\parallel^{in} &= 1 - \frac{\omega_{pe}^2}{\omega^2} - \frac{\delta\omega_{pe}^2}{(\omega - k_\parallel V_b)^2} \\
\epsilon_\perp^{out} &= \epsilon_\perp^{in}(\delta = 0) \\
\epsilon_\parallel^{out} &= \epsilon_\parallel^{in}(\delta = 0)
\end{aligned}$$

In the above equations, δ is defined as n_b/N. The equation of $\epsilon_\parallel^{in} = 0$ is the electrostatic dispersion equation for a homogeneous beam plasma system.

Using the same parameters as the homogeneous beam, we solved Equation (1) numerically. The beam radius a is assumed to be 2.5 m, which is reasonable for the Spacelab 2 experiment (Gurnett et al., 1986). Equation (1) contains solutions for three modes: Cerenkov, cyclotronic, and surface modes (Le Queau et al., 1981). Figure 3 shows that the growth rate for the cyclotronic branch is quite large ($\gamma/\Omega_e \approx 0.25$) and the growth rate of the Cerenkov branch is about one third of the cyclotronic branch. The surface branch has the smallest growth rate among the three branches. As a comparison, the frequency and growth rate of the beam mode for the homogeneous beam plasma system at $\theta = 0^0$ are also plotted in Figure 3

(dotted lines). The frequency of the Cerenkov branch is close to the beam mode frequency. Note that the finite-size effects reduce the growth rate for $k_{||}v_b/\omega_{pe} < 1$.

For a finite-size beam plasma system, the transverse wave numbers are quantized. We found that the transverse wave length outside the beam $(2\pi/k_{\perp}^{out})$ is about one hundred times the beam radius for the cyclotronic branch. Due to lack of space, the results will be discussed separately.

The growth rate at frequencies below Ω_e is very small but interesting. Figure 4, which presents the growth rate in the logarithm scale versus the normalized frequency ω/ω_{pe}, shows the instability extending to frequencies below $\Omega_e = 0.33\omega_{pe}$. The growth rate has a minimum at $\omega = \Omega_e$ and increases with decreasing frequency to a local maximum around $\omega = 0.25\omega_{pe}$. Although the normalized growth rate γ/ω_{pe} is only about 10^{-3} for $\omega < \Omega_e$, the wave amplitude can still grow to twenty times in one milisecond.

4 Discussion

The full electromagnetic dispersion equation is solved for parameters relevant to electron beam experiments from the Space Shuttle. The numerical solutions indicate instabilities for the electron beam and whistler modes. The electron beam mode with frequency $\omega = k_{\parallel} v_b$ has large growth rates over a wide range of frequencies and angles, whereas whistler waves have small growth rates at frequencies near the electron cyclotron frequency. At oblique propagation and at low frequencies ($\omega < 0.1\Omega_e$), the beam mode has a significant electromagnetic component. The dispersion curve for the beam and whistler modes crosses each other, suggesting that the two modes can be easily coupled.

The electromagnetic dispersion relation for a finite-size electron beam is very difficult to solve. We have thus examined the finite-size beam effects in the electrostatic limit. The numerical solutions of the finite-size beam dispersion equation confirm the solutions of electromagnetic dispersion relation of a homogeneous beam, but also exhibit a new and interesting feature.

Our numerical solutions of the finite-size beam dispersion equation agree with the work of Le Queau et al. (1981) when we use their parameters. However, Le Queau et al. (1981) solved the dispersion equation only for frequencies above the electron cyclotron frequency Ω_e. We obtained numerical solutions below the electron cyclotron frequency and found that the instability in fact extends to frequencies below Ω_e with a minimum and negligible growth rate at $\omega = \Omega_e$. This result may explain the Spacelab 2 observations, which show no wave emission near Ω_e (see Figure 1 of Gurnett et al., 1986). Since the beam mode of a homogeneous beam has a large growth rate near $\omega = \Omega_e$ (see Figure 3), the gap of wave emissions near Ω_e cannot be interpreted without invoking finite-size effects.

The present study is motivated by new experimental results from Spacelab 1 and 2 (Taylor et al., 1985; Gurnett et al., 1986). In particular, the remote sub-satellite observations during the Spacelab 2 experiment indicate broadband emissions at frequencies less than the electron cyclotron frequency and narrow band emissions near the electron plasma frequency. The broadband emissions below the electron cyclotron frequency are suggested to be whistler waves propagating near the resonance cone (Gurnett et al., 1986). Because the whistler mode instability occurs at oblique propagation with a small growth rate, it is unlikely that the artificial electron beams fired from the Space Shuttle excite whistler waves directly. However, whistler waves can be generated by other nonlinear processes such as para-

metric decay of the beam mode into the whistler mode. Beating of two high frequency plasma waves can also produce electrostatic waves at frequencies below the electron cyclotron frequency (La Queau et al., 1981). The present work suggests another mechanism of generating whistler waves by the direct coupling of the beam and whistler modes. Mode conversion is known to occur easily when the medium has a density gradient and the dispersion curves of two modes are crossed (Stix, 1965). Therefore, our interpretation of whistler wave emissions by artificial electron beams is that the beam mode at frequencies below the electron cyclotron frequency is converted into the whistler mode at the edge of the electron beam.

Acknowledgement

This work is supported by the Air Force Geophysical Laboratory Contract F19628-85-K-0004 and NASA Contract No. NAS8-32488.

References

Farrell, W. M., D. A. Gurnett, and P. M. Banks, Measurements of the power and efficiency of whistler-mode radiation from the Spacelab-2 electron beam, EOS, 67, 340, 1986

Gurnett, D. A., S. D. Shawhan and R. R. Shaw, Auroral hiss, z-mode radiation, and auroral kilometric radiation in the polar magnetosphere: DE 1 observations, J. Geophys. Res., 88, 329, 1983.

Gurnett, D. A., W. S. Kurth, J. T. Steinberg, P. M. Banks, R. I. Bush and W. J. Raitt, Whistler-mode radiation from the Spacelab 2 electron beam, Geophys. Res. Lett., 13, 225, 1986.

Le Queau, D., R. Pellat, and A. Saint Marc, Electrostatic instabilities of a finite electron beam propagating in a cold magnetized plasma, Phys. Rev. A, 24, 448, 1981.

Shawhan, S. D., G. B. Murphy, P. M. Banks, P. R. Williamson and W. J. Raitt, Wave emissions from dc and modulated electron beams on STS-3, Radio Science, 19, 471, 1984.

Stix, T. H., The Theory of Plasma Waves, McGraw-Hill, New York, 1962.

Stix, T. H., Radiation and absorption via mode conversion in an inhomogeneous collisionless plasma, Phys. Rev. Lett., 15, 878, 1965.

Taylor, W. W. L., and S. D. Shawhan, A test of incoherent Cerenkov radiation for VLF hiss and other magnetospheric emissions, J. Geophys. Res., 79, 105, 1974.

Taylor, W. W. L., T. Obayashi, N. Kawashima, S. Sasaki, M. Yanagisawa, J. L. Burch, D. L. Reasoner, and W. T. Roberts, Wave-particle interactions induced by SEPAC on Spacelab-1: wave observations, Radio Sci., 20, 486, 1985.

Figure Captions

Figure 1 Frequency and growth rate of the electron beam for $\theta = 0°, 30°$ and $60°$ as a function of kc/Ω_e (solid lines). The frequency and growth rate of whistler waves are also plotted as dotted curves for comparison.

Figure 2 The ratio of the longitudinal to the transverse electric field versus kc/Ω_e (top panel). The dispersion curves of the beam and whistler modes are plotted in the bottom panel.

Figure 3 Frequency and growth rate of plasma instabilities of a finite-size elelctron beam as a function of $k_{\|}v_b/\Omega_{pe}$. The curves denoted by 1 are the Cerenkov mode. The surface mode is represented by the curves with the numeral 2 and the cyclotronic mode is represented by the curves with the numeral 3. The frequency and growth rate of the electron beam mode for a homogeneous beam are also plotted as dotted lines.

Figure 4 Normalized growth rate of a finite-size beam in the logarithm scale as a function of the normalized frequency ω/ω_{pe}. The figure shows that the growth rate has a minimum at the electron cyclotron frequency and the instability extends to frequencies below the electron cyclotron frequency.

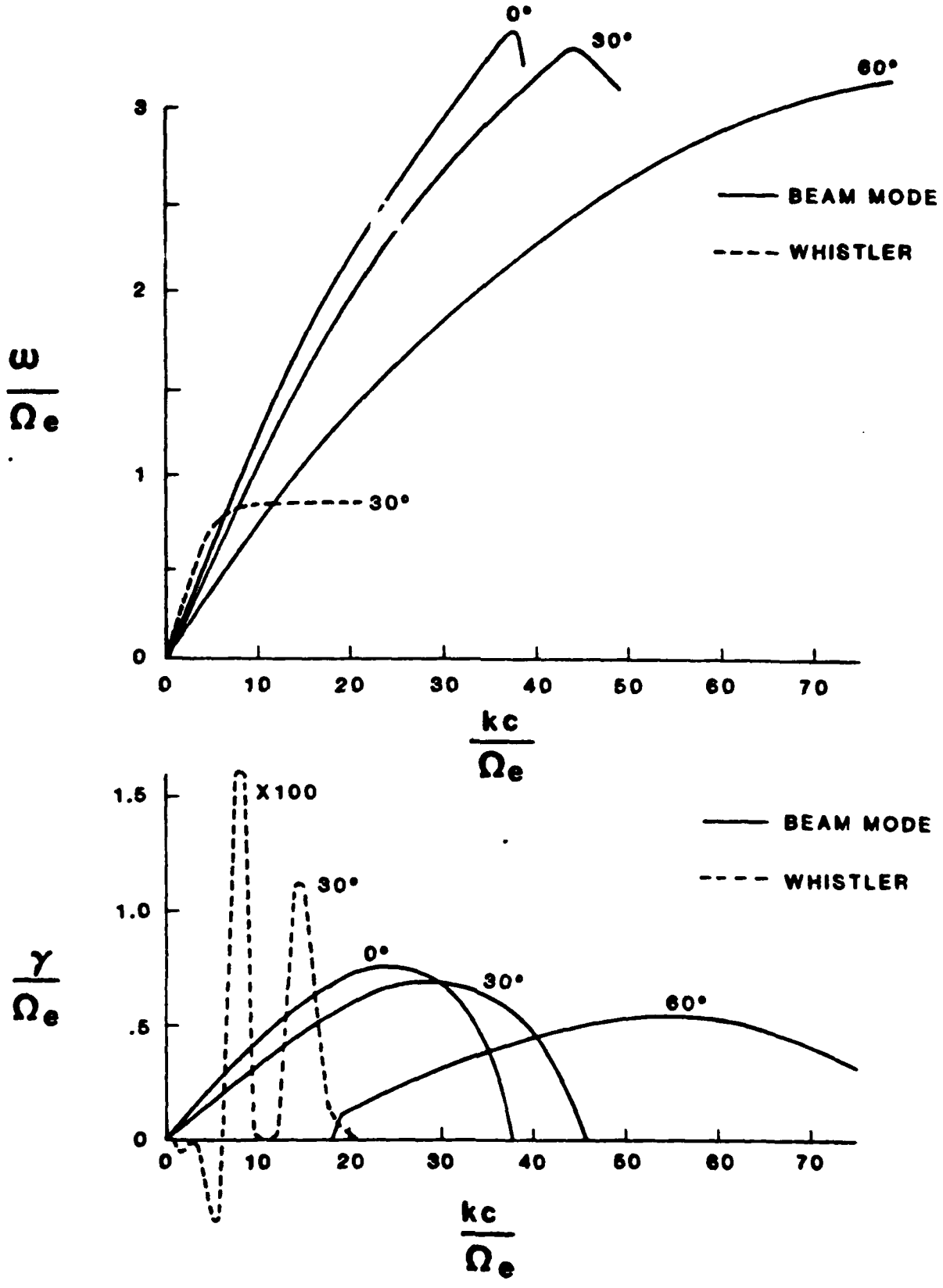
0°
30°
60°
BEAM MODE
WHISTLER
30°
ω/Ωe
kc/Ωe
X100
BEAM MODE
WHISTLER
30°
0°
30°
60°
γ/Ωe
kc/Ωe

FIGURE 1

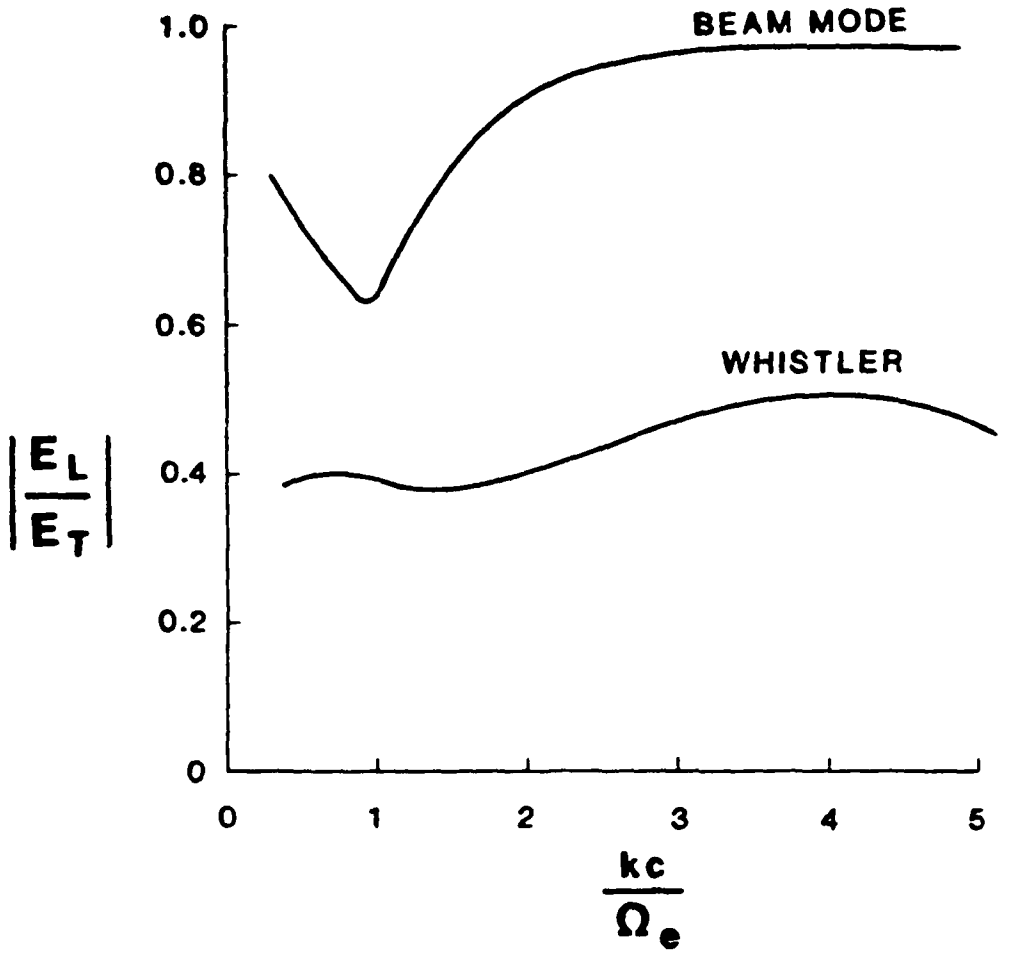
BEAM MODE
WHISTLER
1.0
0.8
0.6
0.4
0.2
0
0
1
2
3
4
5
$\left|\frac{E_L}{E_T}\right|$
$\frac{kc}{\Omega_e}$

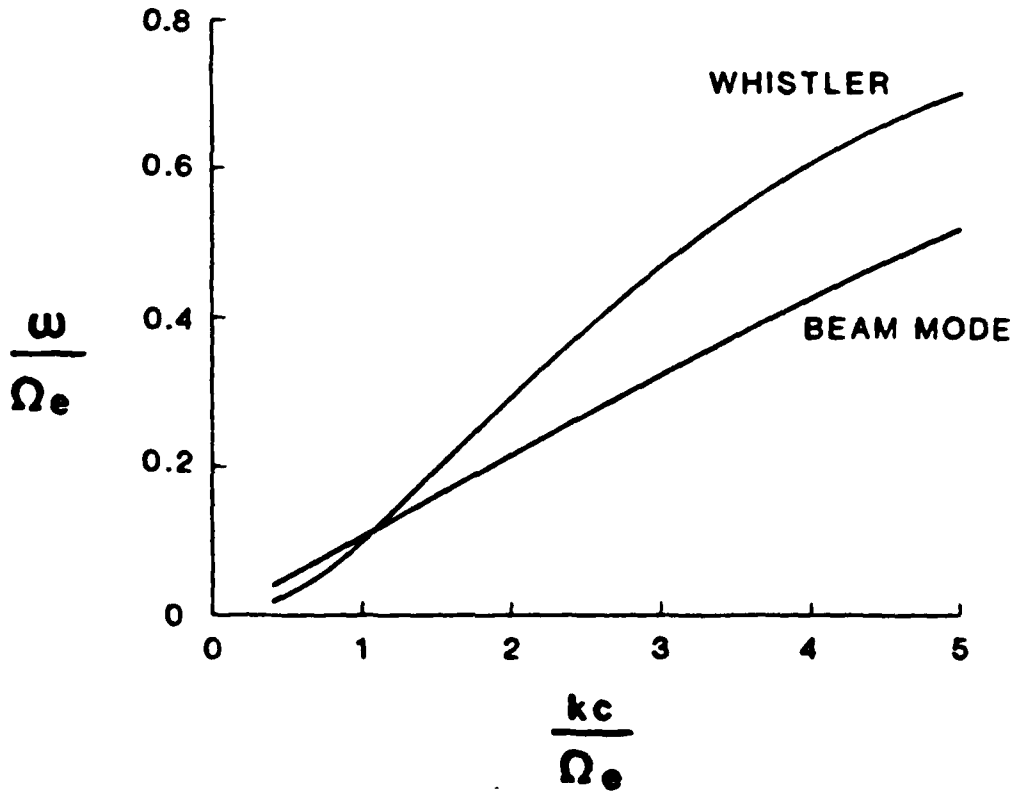
WHISTLER
BEAM MODE
0.8
0.6
0.4
0.2
0
0
1
2
3
4
5
$\frac{\omega}{\Omega_e}$
$\frac{kc}{\Omega_e}$

FIGURE 2

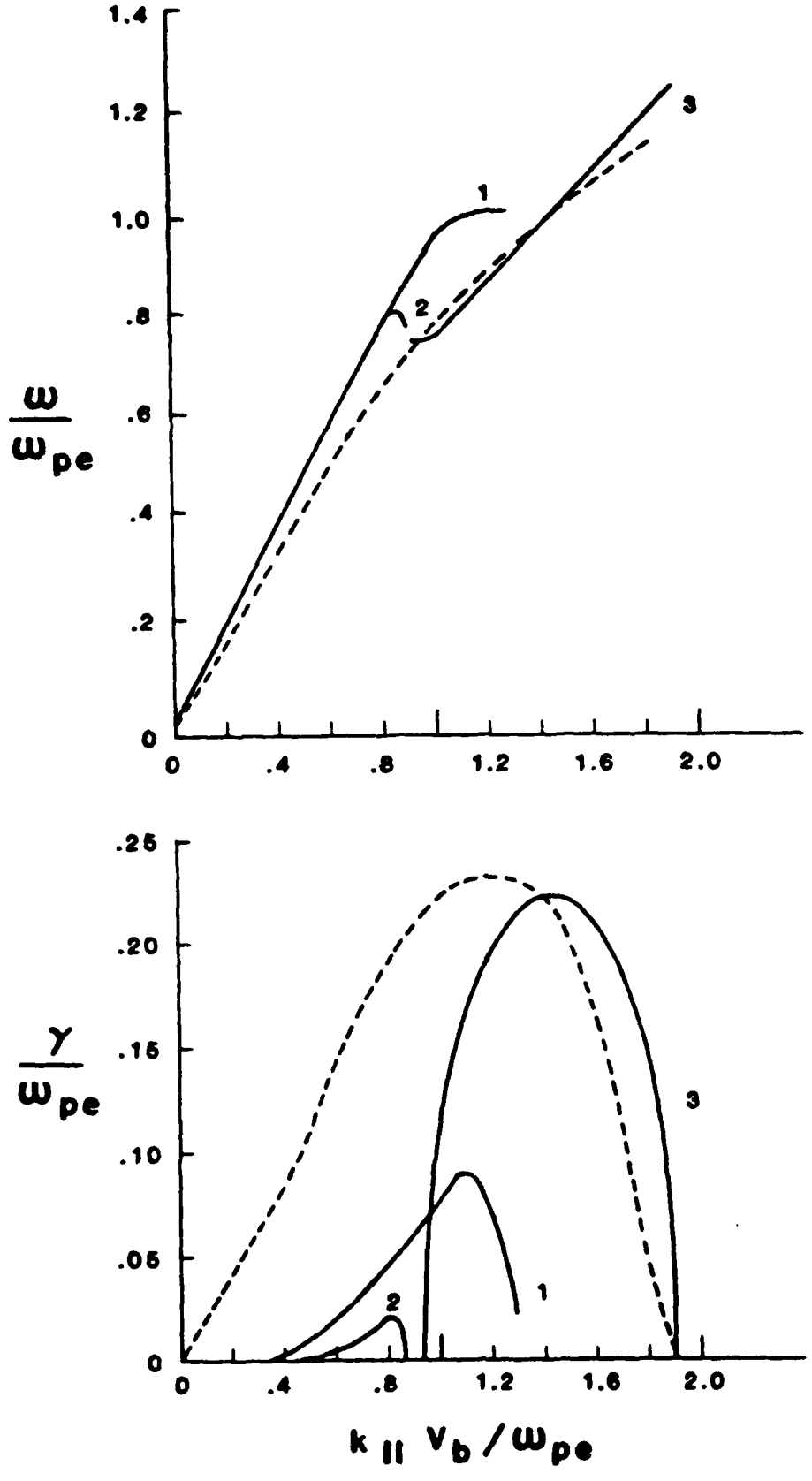
1.4
1.2
1.0
.8
.6
.4
.2
0
ω / ω_pe
1
2
3
0
.4
.8
1.2
1.6
2.0
.25
.20
.15
.10
.05
0
γ / ω_pe
1
2
3
0
.4
.8
1.2
1.6
2.0
k_|| V_b / ω_pe

FIGURE 3

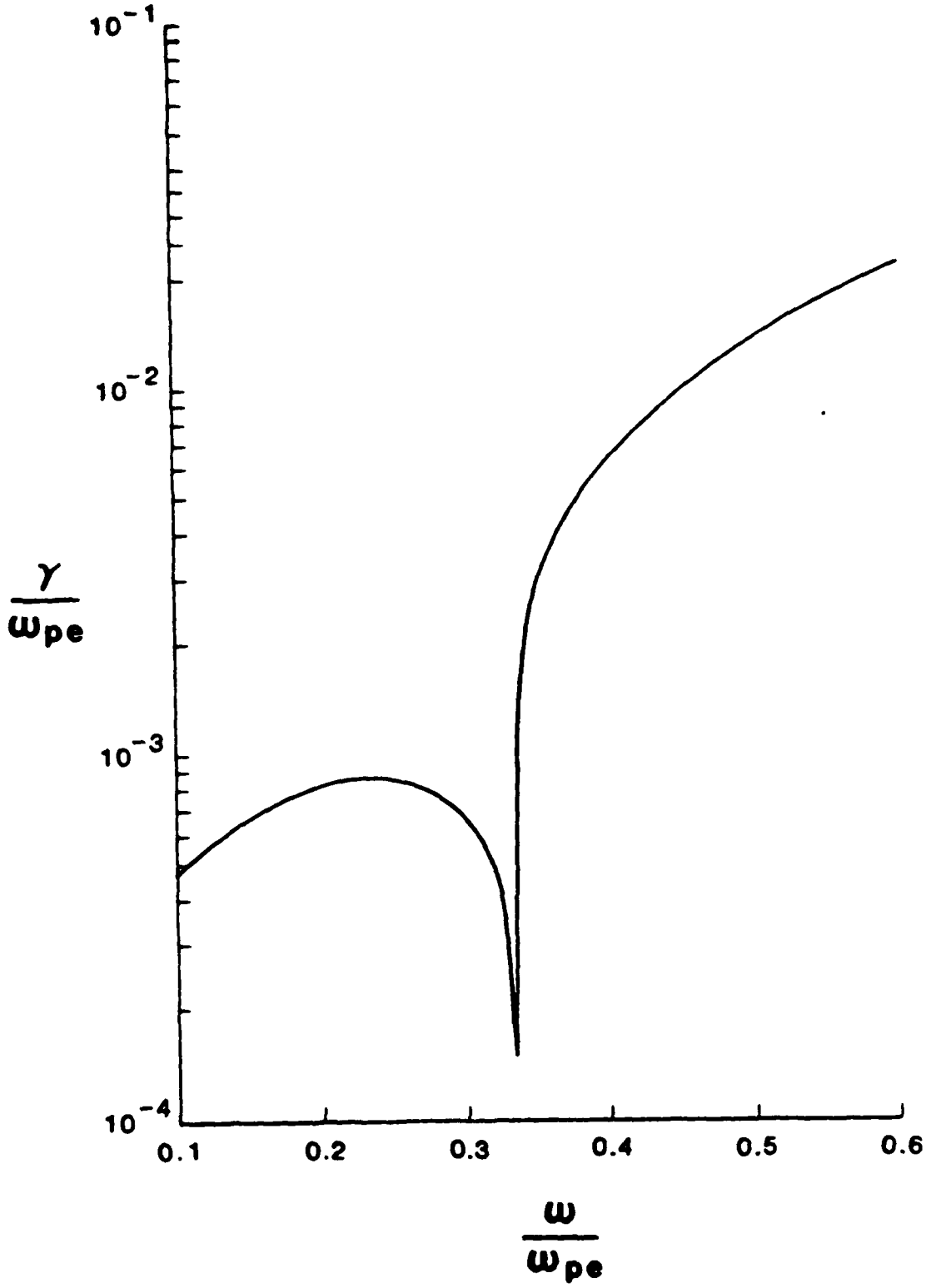
10^{-1}
10^{-2}
10^{-3}
10^{-4}
$\frac{\gamma}{\omega_{pe}}$
0.1
0.2
0.3
0.4
0.5
0.6
$\frac{\omega}{\omega_{pe}}$

FIGURE 4